SCISPACE
formerly Typeset

Open access • Journal Article • DOI:10.1103/PHYSREVE.98.033213

Radiative properties for astrophysical plasma mixtures in nonlocal thermodynamic equilibrium — Source link

Rafael L. Rodríguez, Rafael L. Rodríguez, G. Espinosa, J.M. Gil ...+1 more authors

Institutions: Technical University of Madrid, University of Las Palmas de Gran Canaria

Published on: 28 Sep 2018 - Physical Review E (American Physical Society (APS))

Topics: Thermodynamic equilibrium, Radiative transfer, Astrophysical plasma, Plasma and Order (ring theory)

Related papers:

- Hydrodynamic modelling of accretion impacts in classical T Tauri stars: radiative heating of the pre-shock plasma
- Analysis of radiative opacities for optically thin and thick astrophysical plasmas
- Hydrodynamic Modeling of Accretion Impacts in Classical T Tauri Stars: Radiative Heating of the Pre-shock Plasma
- The radiative transfer of impact broadened spectral lines emitted by an argon plasma described by the local thermodynamic equilibrium appproximation
- Analysis of the influence of the plasma thermodynamic regime in the spectrally resolved and mean radiative opacity calculations of carbon plasmas in a wide range of density and temperature

Share this paper:

View more about this paper here: https://typeset.io/papers/radiative-properties-for-astrophysical-plasma-mixtures-in-3hw88xwdyt

Radiative properties for astrophysical plasma mixtures in nonlocal thermodynamic equilibrium

Rafael Rodríguez,[1,2,*] Guadalupe Espinosa,[1] and Juan Miguel Gil[1,2]
[1]*Departamento de Física, IUNAT, Universidad de Las Palmas de Gran Canaria, 35017 Las Palmas de Gran Canaria, Spain*
[2]*Instituto de Fusión Nuclear, Universidad Politécnica de Madrid, 28006 Madrid, Spain*

(Received 20 June 2018; published 28 September 2018)

Radiative properties play a pivotal role in astrophysical plasma flows and are needed in radiation-hydrodynamic simulations in order to understand their behavior and also to interpret the plasma emission spectra, which are valuable diagnostic tools. Radiative properties of astrophysical plasma mixtures have been commonly calculated for low-density optically thin plasmas assuming coronal equilibrium and for high density assuming local thermodynamic equilibrium. However, there are wide ranges of conditions in which these thermodynamic regimes are not achieved and the plasma is in the nonlocal thermodynamic equilibrium regime. In the present work, a study of the plasma radiative properties of oxygen and iron and an astrophysical plasma mixture in nonlocal thermodynamic steady-state equilibrium is carried out. The ranges of electron temperatures and densities considered are 1–1000 eV and 10^{11}–10^{20} cm^{-3}, respectively. In the study, departures from coronal and local thermodynamic equilibria in terms of the density and temperature are also analyzed. Large differences in the radiative properties that can reach two orders of magnitude when the plasma is far from these thermodynamic regimes are obtained. These analyses are done assuming the plasma to be optically thin. A brief study of the influence of the plasma self-absorption in the radiative properties of oxygen and iron is made. For that purpose, the plasma is assumed with planar geometry and the study is performed in terms of the width of the plasma slab and electron temperature and density.

DOI: 10.1103/PhysRevE.98.033213

I. INTRODUCTION

In almost all astrophysical fluid flows, the radiative properties play a significant role and their accurate calculation is needed to understand their behavior. Optically thin, hot, low-density plasmas, such as those found in interstellar and intergalactic media and stellar wind [1] or in coronal loops in stars [2,3], cool efficiently and their correct hydrodynamic simulation implies an accurate calculation of their cooling rates. Computations of these rates have been carried out in many works both in astrophysics [1,4–9] and in magnetic fusion [10–14] contexts. In general, in these calculations, the plasma was assumed to be in coronal equilibrium (CE) [15], a plasma thermodynamic regime reached by optically thin plasmas at very low densities. In this regime, the cooling rates are density independent. On the other hand, the opacities are fundamental in the transport of radiation through the plasma as in, for example, the stellar evolution and pulsation, in the nuclear reactions in the solar plasma, and in the neutrino flux and solar luminosity. Furthermore, the opacities couple radiative transfer equations to hydrodynamic or magneto-hydrodynamic equations and for this reason they are needed for radiation hydrodynamic simulations. Much effort has been devoted and continues to calculating them, predominantly in the local thermodynamic equilibrium (LTE) regime, which is in general reached at rather high densities. Exhaustive and accurate opacity tables in LTE have been developed, for example, the Opacity Project (OP) [16–18], the OPAL tables [19,20], and those based on using codes such as LEDCOP [21], OPAS [22], and ATOMIC [23]. Moreover, there are also many works to calculate and analyze LTE opacities of different single elements of interest in the range of plasma conditions found in astrophysical scenarios [24–34].

For many density and temperature conditions, the plasmas are in the non-LTE (NLTE) regime and the radiative properties may be noticeably different from those obtained assuming CE and LTE. In NLTE, their calculation is more complicated since there is no *a priori* expression for the occupation probabilities of bound states and they must be obtained by using the so-called collisional-radiative (CR) models [35], which implies solving large sets of rate equations that involve ATOMIC processes that couple ATOMIC configurations, free electrons, and photons. Atomic state-space completeness is a critical aspect of a credible CR model, although its achievement is difficult or even impossible [36]. Therefore, the choice of the state space must be done carefully and it depends on the plasma conditions under analysis. Thus, for example, for plasmas under high intense radiation fields, atomic configurations with inner shells open should be included, whereas for plasmas at moderated densities, ruled by collisions with thermal electrons, the number of double and single configurations can be limited [36]. Another critical issue in the CR models is the degree of atomic description. For low- and intermediate-Z plasmas, detailed level accounting (DLA) or term accounting models including large degrees of configuration interaction are used. For high-Z elements, those approaches become sometimes intractable. In this case, statistic approaches involving grouping of levels into configurations such as the detailed configuration account (DCA)

*rafael.rodriguezperez@ulpgc.es

 ©2018 American Physical Society

approach or grouping configurations into superconfigurations (superconfiguration account approach), combined with the unresolved transition array (UTA) [37] and supertransition array [38] formalisms, respectively, have been shown to be very useful. However, these statistical methods may lack the accuracy to describe isolated levels or transitions. For this reason, hybrids methods that mix detailed and statistical descriptions have been developed [39,40] which present the advantage of retaining the fine description only for the most relevant transitions in a given transition array. However, when the purpose of the radiative properties calculation is to obtain databases for wide ranges of plasma conditions that cover low, intermediate, and high electron densities and temperatures, a balance between completeness and computational complexity must be achieved, especially in the NLTE regime.

In this work, we present a study of the NLTE effects in the calculation of the average ionization, the charge-state distribution, the cooling coefficients, and the Planck and Rosseland mean opacities of plasma mixtures found in astrophysical scenarios. The chemical elements considered in the plasma mixture are H, He, C, N, O, Ne, Na, Mg, Al, Si, S, Ar, Ca, and Fe. Two sets of solarlike abundances [41,42] are employed in order to compare with other simulations. The calculations and the analysis are carried out in ranges of electron temperatures and densities of 1–1000 eV and 10^{11}–10^{20} cm^{-3}, respectively. These ranges of plasma conditions include several astrophysical objects such as hot gas in supernova remnants, active galactic nuclei [8], stellar winds [1], accretion shocks in young stars [43], stellar coronal loops [2], and stellar envelopes [31], among others. Furthermore, we also analyze the cooling rates and mean opacities for two single elements of the mixture, oxygen and iron. They present a relevant contribution to these properties in the mixture for different ranges of temperatures. In addition, their study serves to illustrate the behavior, with the electron density and temperature, for the other chemical elements of the mixture with similar atomic number and provides an understanding of the results obtained for the whole mixture.

Due to the wide range of plasma conditions simulated, we employ a statistical atomic description based on the DCA and UTA approaches in order to achieve a compromise between atomic description and computational costs. Therefore, the main aim of this work is not to present precise values for the radiative properties but to determine the influence of the NLTE regime in their calculation and to analyze the departures from CE and LTE as a function of the plasma conditions, estimating their differences with respect to CE or LTE calculations. This analysis will allow determining in which range of plasma densities and temperatures these properties should be calculated in NLTE, which is very relevant when databases of radiative properties are needed in a wide range of plasma conditions for radiation-hydrodynamic simulations. A further step would imply improving the atomic description to simulate the radiative properties more precisely in those ranges of plasma conditions of interest in which the NLTE effects are determinant. In either case, the values of the radiative properties, calculated in the LTE regime, provided by our model generally have relative differences lower than 50% when they are compared to LTE simulations carried out with codes based on more detailed atomic descriptions, as shown in Sec. III. These differences are considerably smaller than those obtained between LTE and NLTE calculations when the plasma is far from the LTE regime, where the disagreement can reach two orders of magnitude. The previous analyses were performed assuming the plasma to be optically thin. This work ends with a brief study of the influence of the plasma self-absorption, as a function of the plasma geometrical thickness, in the calculation of the radiative properties for oxygen and iron.

The paper is structured as follows. In Sec. II the theoretical and computational models used for the simulations are presented. Section III is devoted to the results obtained and is divided into four parts. In Sec. III A comparisons with other NLTE models are presented. Sections III B and III C are devoted to the analysis of NLTE effects in the calculation of the radiative properties of iron, oxygen, and the plasma mixture and also to study the departures from CE and LTE with density and temperature. In Sec. III D the analysis of the influence of the plasma self-absorption on these plasma properties is presented. Section IV summarizes and discusses the results.

II. THEORETICAL AND COMPUTATIONAL MODELS

The atomic state populations of plasmas in NLTE are usually determined using a CR model. In this case, the populations of the atomic levels in the plasma are obtained by solving a set of rate equations given by

$$\frac{dN_{\zeta i}(\mathbf{r},t)}{dt} = \sum_{\zeta' j} N_{\zeta' j}(\mathbf{r},t) R^{+}_{\zeta' j \to \zeta i} - \sum_{\zeta' j} N_{\zeta i}(\mathbf{r},t) R^{-}_{\zeta i \to \zeta' j}, \tag{1}$$

where $N_{\zeta i}$ is the population density of the atomic configuration or level i (depending on the atomic approach) of the ion with charge state ζ. The terms $R^{+}_{\zeta' j \to \zeta i}$ and $R^{-}_{\zeta' j \to \zeta i}$ take into account all the atomic processes, both collisional and radiative, which contribute to populate and depopulate the atomic configuration ζi, respectively. These atomic processes are responsible for the atomic level population distribution in the plasma. When the characteristic time of the most relevant atomic process in the plasma is considerably shorter than the characteristic time of plasma evolution, i.e., the time associated with changes in the plasma density and temperature, then one could consider that the atomic processes occur under constant values of plasma density and temperature or, equivalently, that the atomic processes are fast enough to distribute the atomic level populations in the plasma before the density and temperature of the plasma change. When this condition is fulfilled the plasma can be considered in steady state. Obviously, for those plasmas in which the density or temperature evolves rapidly over time, the steady-state approach may not be accurate enough. On the other hand, the steady-state approach is commonly used to calculate the plasma atomic level populations needed to generate radiative properties databases in wide ranges of plasma conditions for radiation-hydrodynamics simulations and in the present work the plasma level populations are obtained by solving the rate equations of the CR model in steady state (CRSS). In this situation, the time derivative in Eq. (1) vanishes and the set

of rate equations that must be solved is given by

$$\sum_{\zeta' j} N_{\zeta' j}(\mathbf{r},t) R^{+}_{\zeta' j \to \zeta i} - \sum_{\zeta' j} N_{\zeta i}(\mathbf{r},t) R^{-}_{\zeta i \to \zeta' j} = 0. \quad (2)$$

The atomic calculations in this work are carried out based on the relativistic detailed configuration accounting (RDCA) approach and therefore $N_{\zeta i}$ denotes a relativistic atomic configuration. Two complementary equations have to be satisfied together with Eq. (2): first, the requirement that the sum of all the partial densities equals the total ion density $n_{\rm ion}$,

$$\sum_{\zeta=0}^{Z} \sum_{i=0}^{M_\zeta - 1} N_{\zeta i} = n_{\rm ion}, \quad (3)$$

and second, the charge neutrality condition in the plasma

$$\sum_{\zeta=0}^{Z} \sum_{i=0}^{M_\zeta - 1} \zeta N_{\zeta i} = n_e, \quad (4)$$

where M_ζ is the total number of levels for the charge state ζ and n_e is the electron density. The plasma average ionization is defined as

$$\overline{Z} = \frac{\sum_{\zeta=0}^{Z} \zeta N_\zeta}{\sum_{\zeta=0}^{Z} N_\zeta} = \frac{n_e}{n_{\rm ion}}. \quad (5)$$

For a given condition of density and temperature, the resolution of the rate equations also provides the plasma charge-state distribution (CSD), which is defined as the set of the population densities $\{N_\zeta\}$ of the ions present in the plasma. The atomic processes included in the present CRSS model, when the plasma is assumed to be optically thin, are collisional ionization [44] and three-body recombination, spontaneous decay [45], collisional excitation [46] and deexcitation, radiative recombination [47], autoionization, and electron capture (obtained from the collisional excitation cross section [48]). The rates of the inverse processes are obtained through the detailed balance principle. It is assumed that the collision times between ions and electrons are short enough so the ions can be considered to be at rest. The effect of the plasma environment on the population of the atomic levels is modeled through the depression of the ionization potential or continuum lowering (CL). The application of the CL can restrict the number of bound states available and in this work the formulation developed by Stewart and Pyatt [49] is applied.

In the calculation of the rates of the atomic processes, a Maxwell-Boltzmann distribution for the free electrons is assumed. The characteristic time for the electrons to thermalize is given by the average time between electron-electron collisions [50,51]

$$\tau_{ee} = \frac{2\pi\epsilon_0^2}{e^4} \frac{m_e^{1/2} T_e^{3/2}}{n_e \ln\Lambda}, \quad (6)$$

where e, m_e, and T_e are the electron charge, mass, and temperature, respectively, ϵ_0 is the vacuum permittivity, and Λ is given by

$$\Lambda = \frac{3}{2}\left(\frac{\epsilon_0^3 T_e^3}{\pi n_e e^6}\right)^{1/2}. \quad (7)$$

TABLE I. Free-electron mean free paths λ_{ee} between electron-electron collisions calculated for several plasma conditions of the range analyzed in this work. The electron density is given in cm^{-3}, the electron temperature in eV, and λ_{ee} in m.

T_e	$n_e = 10^{11}$	$n_e = 10^{14}$	$n_e = 10^{17}$	$n_e = 10^{20}$
50	2.25×10^{2}	2.58×10^{-1}	3.03×10^{-4}	3.67×10^{-7}
200	3.33×10^{3}	3.79×10^{0}	4.39×10^{-3}	5.21×10^{-6}
350	9.92×10^{3}	1.12×10^{1}	1.29×10^{-2}	1.52×10^{-5}
500	2.00×10^{4}	2.25×10^{1}	2.58×10^{-2}	3.03×10^{-5}
650	3.32×10^{4}	3.74×10^{1}	4.29×10^{-2}	5.02×10^{-5}
800	4.97×10^{4}	5.61×10^{1}	6.41×10^{-2}	7.49×10^{-5}
1000	7.69×10^{4}	8.65×10^{1}	9.88×10^{-2}	1.15×10^{-4}

The electron mean free paths can be estimated using these average times and the electron velocities obtained from the mean energies associated with the electron temperatures of the Maxwell-Boltzmann distributions. We have calculated the electron mean free paths for several plasma conditions analyzed in this work assuming nonrelativistic plasmas and they are listed in Table I. This property provides an estimation of the average plasma volume needed for the free electrons to thermalize. In our NLTE simulations we assume homogeneous plasmas (in density and temperature). As expected, the mean free path decreases with the electron density and increases with the electron temperature. Since the electron mean free paths are obtained from the mean electron energies, for a given electron temperature listed in the table there would be electrons that need larger mean free paths to thermalize. For those situations in which substantial deviations from a Maxwell-Boltzmann distribution for the free electrons are produced, the free-electron energy distribution functions are usually obtained from a simultaneous solution of the time-dependent atomic rate equations and Boltzmann electron kinetics [52]. This kind of simulation is tractable when a specific situation is simulated but not when the interest is focused on the determination of a large number of mean radiative properties in a wide range of plasma conditions. In this case, thermal distributions for the free electrons are commonly assumed, as in this work.

On the other hand, when the electron density is very high the exchange effects are relevant and then the Fermi-Dirac distribution should be used instead of the Maxwell-Boltzmann one to describe the electron distribution. The former reduces to the latter when the chemical potential $\mu \to -\infty$ and this implies the criterion [15]

$$\frac{n_e}{2}\left(\frac{2\pi(\hbar c)^2}{m_e c^2 T_e}\right)^{3/2} \ll 1, \quad (8)$$

where c is the speed of light and $\hbar$ is Planck's constant divided by 2π. We apply this criterion for the range of plasma conditions considered in this work and even at the most unfavorable plasma condition (lowest electron temperature and highest electron density) the criterion is fulfilled and therefore the use of the Maxwell-Boltzmann distribution seems adequate for the range of plasma conditions analyzed.

For optically thick plasmas, the rate equations would be coupled to the radiative transfer equation. In this work, the

nonlocal radiation transport effects are included in the rate equations using the escape factor formalism [53]. This formalism avoids the need to perform a simultaneous calculation of radiative transport and atomic physics and also uncouples the radiative transfer and rate equations. For a given line transition $\zeta i \leftrightarrow \zeta j$, the escape factor Λ_{ji} is introduced as an alternative way of writing the net rate of line emission and it leads to an effective reduction in the Einstein spontaneous emission coefficient $A_{\zeta j\rightarrow\zeta i}$, which is written as $\Lambda_{ji}A_{\zeta j\rightarrow\zeta i}$. To compute the escape factors for the three basic geometries, planar, cylindrical, and spherical, the technique described in [53] is adopted, assuming a uniform distribution for emitting atoms and isotropic emission. The escape factor is written as

$$\Lambda_{ji} = \int_0^\infty \phi_{ij}(\nu)\frac{1}{\tau_{ij}(\nu)}F[\tau_{ij}(\nu)]d\nu. \tag{9}$$

The optical depth is $\tau_{ij}(\nu) = \kappa_{\zeta i\rightarrow\zeta j}(\nu)L$, where L denotes the characteristic plasma dimension, i.e., slab width, cylinder, or sphere radius. Finally, $F[\tau_{ij}]$ is a functional of the optical depth whose particular form depends on the considered geometry.

Multicomponent plasmas are considered in the present work. As mentioned above, the chemical elements included in the plasma mixture are H, He, C, N, O, Ne-Si, S, Ar, Ca, and Fe, where Ne-Si denotes all the elements from Ne to Si. For a given electron density and temperature, the CRSS model is solved for each element. Collisional processes that connect ions of different chemical species are not included. However, as the different elements of the multicomponent plasma are immersed in a common pool of free electrons, they will be coupled through the electron density since the plasma level population (and the average ionization) of each component has to be consistent with the same electron density, which ensures the electrical equilibrium keeping the overall plasma neutrality [54,55]. The CRSS model described is implemented in the numerical code MIXKIP [56].

The atomic structure (relativistic energy levels, wave functions, and oscillator strengths) and the photoionization cross sections were calculated using the FAC code [45], in which a fully relativistic approach based on the Dirac equation is used. Hence, the atomic levels of an atomic ion are obtained by diagonalizing the relativistic Hamiltonian. In the RDCA approach, the transition energies include the UTA shifts [37]. With respect to the set of configurations, we include those with an energy within two times the ionization energy of the ground configuration of the ion.

Once the plasma level populations have been computed, the plasma radiative properties are calculated using the RAPCAL code [57,58], which is implemented in MIXKIP. The monochromatic emissivity and absorption are denoted in this work by $j(\nu)$ and $\kappa(\nu)$, respectively (where we have omitted the dependence on the position and time to simplify the notation), and both of them include the bound-bound, bound-free, and free-free contributions

$$j(\nu) = j_{bb}(\nu) + j_{bf}(\nu) + j_{ff}(\nu), \tag{10}$$

$$\kappa(\nu) = \kappa_{bb}(\nu) + \kappa_{bf}(\nu) + \kappa_{ff}(\nu), \tag{11}$$

where ν is the photon frequency. The bound-bound contribution to the emissivity is given by

$$j_{bb}(\nu) = \sum_\zeta \sum_{i,j} j_{\zeta j\rightarrow\zeta i}(\nu), \tag{12}$$

with

$$j_{\zeta j\rightarrow\zeta i}(\nu) = \frac{h\nu}{4\pi}N_{\zeta j}A_{\zeta j\rightarrow\zeta i}\phi_{ij}(\nu), \tag{13}$$

where h is Planck's constant. The radiative transitions rates in FAC are calculated in the single multipole approximation, and in this work they are obtained in the electric dipole approach. The oscillator strengths include a correction to take into account configuration interaction effects due to the mix between relativistic configurations that belong to the same nonrelativistic one. The bound-bound contribution to the absorption is given by

$$\kappa_{bb}(\nu) = \sum_\zeta \sum_{i,j} \kappa_{\zeta i\rightarrow\zeta j}(\nu), \tag{14}$$

with

$$\kappa_{\zeta i\rightarrow\zeta j}(\nu) = \frac{h\nu}{4\pi}N_{\zeta i}\frac{g_{\zeta j}}{g_{\zeta i}}\frac{c^2}{2h\nu_{ij}^3}A_{\zeta j\rightarrow\zeta i}\phi_{ij}(\nu)\left(1-\frac{g_{\zeta i}}{g_{\zeta j}}\frac{N_{\zeta j}}{N_{\zeta i}}\right), \tag{15}$$

where $g_{\zeta i}$ and $g_{\zeta j}$ are the statistical weights of the i and j relativistic configurations, respectively. In the previous equations, $\phi_{ij}(\nu)$ represents the line profile for both line emission and absorption since in this work a complete redistribution hypothesis is assumed [59]. In the evaluation of the line profile, natural, Doppler, electron-impact [60], and UTA broadenings are included. The line-shape function is applied with the Voigt profile which incorporates all these broadenings.

The bound-free contribution to the emissivity is determined by means of

$$j_{bf}(\nu) = \sum_{\zeta,i} \sum_{\zeta,j} j_{\zeta+1j\rightarrow\zeta i}(\nu), \tag{16}$$

with

$$j_{\zeta+1j\rightarrow\zeta i}(\nu) = \frac{h^4 n u^3 N_{\zeta+1j}n_e f(\varepsilon)}{2^{5/2}\pi c^2 m_e^{3/2}\varepsilon^{1/2}}\frac{g_{\zeta i}}{g_{\zeta+1j}}\sigma^{\rm pho}_{\zeta i\rightarrow\zeta+1j}(\nu), \tag{17}$$

where ε is the energy of the free electron and m_e is the electron mass. In this work, a Maxwell-Boltzmann distribution $f(\varepsilon)$ at temperature T_e for the free electrons is assumed. The photoionization cross section $\sigma^{\rm pho}_{\zeta i\rightarrow\zeta+1j}(\nu)$ is calculated using the FAC code in the relativistic distorted-wave approach. For the bound-free spectra, the DCA approximation is used as well. The bound-free contribution to the absorption is given by

$$\kappa_{bf}(\nu) = \sum_{\zeta,i} \sum_{\zeta,j} \kappa_{\zeta i\rightarrow\zeta+1j}(\nu), \tag{18}$$

with

$$\kappa_{\zeta i\rightarrow\zeta+1j}(\nu) = N_{\zeta i}\sigma^{\rm pho}_{\zeta i\rightarrow\zeta+1j}(\nu)\left(1-\frac{N_{\zeta+1j}n_e f(\varepsilon)g_{\zeta i}}{N_{\zeta i}g_{\zeta+1j}g(\varepsilon)}\right), \tag{19}$$

where $g(\varepsilon)$ is the density of states with energy ε, which, assuming an ideal gas of free electrons, is given by

$$g(\varepsilon) = 4\pi\left(\frac{2m_e}{h^2}\right)^{3/2}\varepsilon^{1/2}. \quad (20)$$

For the free-free contributions to the emissivity and the absorption, the Kramers semiclassical expression for the inverse bremsstrahlung cross section is used [61]:

$$\sigma_\zeta^{\mathrm{IB}}(\nu) = \frac{16\pi^2 e^2 h^2 \alpha}{3\sqrt{3}(2\pi m_e)^{3/2}}\frac{\zeta^2 n_e}{T_e^{1/2}(h\nu)^3}. \quad (21)$$

Assuming a Maxwell-Boltzmann distribution for the free electrons, we obtain

$$j_{ff}(\nu) = \frac{32\pi^2 e^4 a_0^2 \alpha^3}{\sqrt{3}(2\pi m_e)^{3/2}h}\left(\frac{m_e}{2\pi T_e}\right)^{1/2}\overline{Z^2}n_{\mathrm{ion}}n_e e^{-h\nu/T_e}, \quad (22)$$

$$\kappa_{ff}(\nu) = \frac{16\pi^2 e^2 h^2 \alpha}{3\sqrt{3}(2\pi m_e)^{3/2}}\frac{\overline{Z^2}n_{\mathrm{ion}}n_e}{T_e^{1/2}(h\nu)^3}(1 - e^{-h\nu/T_e}). \quad (23)$$

In order to determine the opacity $k(\nu)$, the absorption due to the scattering of photons is also taken into account. In RAPCAL this one is approximated using the Thomson scattering cross section [62]

$$\kappa_{\mathrm{scatt}} = n_e\sigma^{\mathrm{Thom}}, \quad (24)$$

with $\sigma^{\mathrm{Thom}} = 6.65 \times 10^{-25}$ cm^2. Finally, the opacity is given by

$$k(\nu) = \frac{1}{\rho}[\kappa(\nu) + \kappa_{\mathrm{scatt}}], \quad (25)$$

with ρ the density of matter. As said before, RAPCAL also provides the Planck k_P and Rosseland k_R mean opacities, which are given by [63]

$$k_P = \int_0^\infty d\nu\, \tilde{B}(\nu, T)[k(\nu) - \kappa_{\mathrm{scatt}}/\rho], \quad (26)$$

$$\frac{1}{k_R} = \int_0^\infty d\nu \frac{\partial\tilde{B}(\nu, T)}{\partial T}\frac{1}{k(\nu)}, \quad (27)$$

where $\tilde{B}(\nu, T)$ is the normalized Planckian function

$$\tilde{B}(\nu, T) = \frac{15}{\pi^4 T}\frac{u^3}{e^u - 1}, \quad u = \frac{h\nu}{T}. \quad (28)$$

The radiative power loss (RPL) is evaluated as

$$P = 4\pi\int_0^\infty j(\nu)d\nu \quad (29)$$

and the cooling rate is obtained as the ratio between the RPL and the electron and ion particle densities.

III. RESULTS

A. Comparison with nonlocal thermodynamic equilibrium codes

Plasma properties of some of the chemical elements involved in the plasma mixture analyzed in this work have already been tested with other simulations in both the LTE and NLTE regimes for plasma conditions of present interest. Thus, in a previous work, we studied the plasma thermodynamic regimes of optically thin steady-state carbon plasmas [64] in the range of electron temperatures and densities of 1–1000 eV and 10^{10}–10^{22} cm^{-3}, respectively, and their influence in the determination of the radiative properties. Our simulations for the monochromatic, multigroup, and mean opacities [65] and the average ionization and cooling rates [13] were also tested. For aluminum plasmas, we determined the plasma thermodynamic regimes as a function of plasma conditions and checked our simulations for the average ionization, CSDs, mean opacities, and monochromatic opacities and emissivities with other LTE and NLTE simulations [57,66]. Finally, we performed comparisons of the average ionization, CSDs, and RPLs of argon plasmas [56] with NLTE codes from [67], for electron temperatures from 3 to 35 eV and at the electron densities 10^{16} and 10^{20} cm^{-3}. The results obtained in all these studies were quite acceptable. In this section, we present comparisons with other NLTE simulations for plasmas of neon and iron, which are also relevant chemical elements in astrophysical mixtures, to complement the testing previously done for the other elements.

TABLE II. Comparison of the average ionization and radiative power loss (in ergs s^{-1} cm^{-3}) of a neon plasma at two electron temperatures (in eV) at an electron density of 10^{18} cm^{-3}, with calculations of codes from [68].

	Average ionization		Radiative power loss	
Code	$T_e = 5$	$T_e = 40$	$T_e = 5$	$T_e = 40$
MIXKIP	2.01	7.29	8.10×10^{14}	3.26×10^{15}
code 1	2.20	7.21	1.82×10^{15}	4.55×10^{15}
code 2	2.19	7.36	1.94×10^{14}	4.31×10^{15}
code 3	2.06	7.76	7.08×10^{14}	1.99×10^{15}
code 4	2.01	7.16	3.85×10^{14}	4.05×10^{15}

In Table II we have listed the average ionization and the radiative power loss for neon plasmas calculated with MIXKIP at the electron density of 10^{18} cm^{-3} and for two electron temperatures, 5 and 40 eV. They are compared with calculations from NLTE kinetic codes from [68]. From the table we observe that MIXKIP provides values similar to those obtained by the other codes, with relative differences between 2.5% and 9.5% for the average ionization at an electron temperature of 5 eV and between 1.8% and 6.5% at 40 eV. With respect to the RPL, larger discrepancies between the values provided by the different codes are detected. Thus, at a temperature of 5 eV relative differences between 12.6% and 60% are found. For the higher temperature, these range from 22% to 40%. These disagreements are expected, due to different atomic descriptions and configurations considered in each code. Since the RPL is more sensitive than the average ionization to these issues, the discrepancies obtained are larger.

In Fig. 1 we present comparisons of the RPLs and the average ionizations calculated with the MIXKIP code for iron plasmas with those obtained with NLTE codes from [69], at two electron densities, 10^{14} and 10^{19} cm^{-3} and electron temperatures from 30 to 1000 eV. The average ionizations range from 6 to 18 and from 9 to 19 for the lowest and highest densities, respectively. The figure shows that, for both properties, the discrepancies between the codes for the lowest density

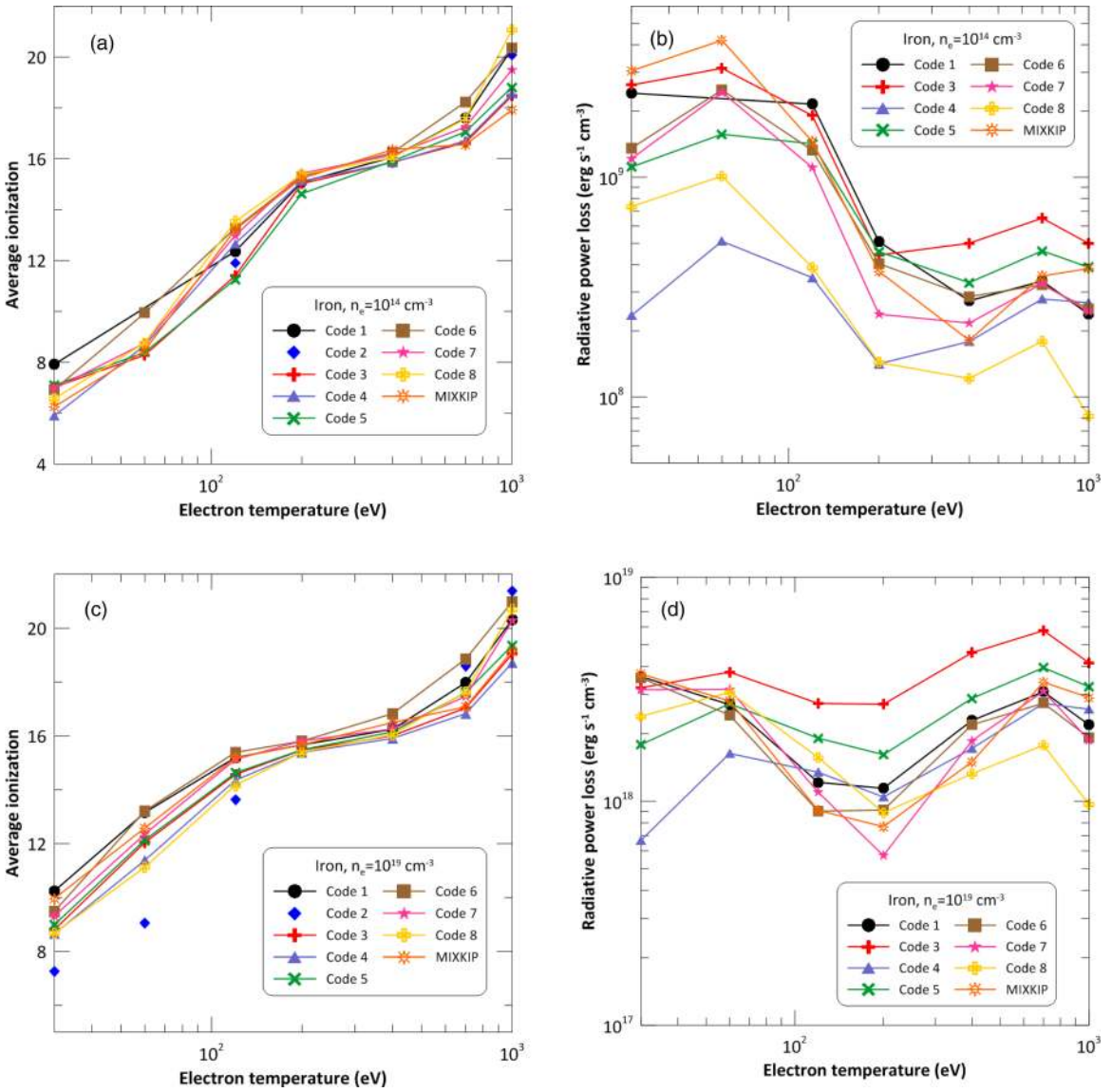

FIG. 1. Comparison of the average ionization and radiative power loss of iron plasmas at two electron densities, with calculations of codes from [69].

are in general slightly greater than for the highest. Thus, for the average ionization, the relative differences are typically between 1% and 10% for both densities but at 10^{19} cm^{-3} most of the relative differences are lower than 5%. With respect to the RPLs, the relative differences between codes in general range from 50% to 100% for both densities, although for some codes we detected relatives differences that can reach 400% for some plasma conditions. The greater discrepancies obtained at 10^{14} cm^{-3} may be due to the autoionization and the dielectronic recombination process contributions, which are more relevant at low densities, and their corresponding rates varied significantly between the codes [67]. At higher densities the collisional processes are dominant and this could decrease the differences.

From Figs. 1(a) and 1(c) we detect better agreement among all the codes for electron temperatures from 200 to 300 eV, where a plateau for an average ionization around 16 (Ne-like ion) is obtained. Thus, for example, the relative differences between the RPLs provided by the different codes are always lower than 30%. The most abundant ion is Ne, which is a closed-shell ion whose atomic structure is simpler than for ions with partially occupied shells, which can explain the better agreement observed. As shown in Fig. 1, the behavior of the average ionization and the RPL with the density and temperature obtained with the MIXKIP code are similar to most of the other codes and also their values.

B. Departures from coronal equilibrium

Coronal equilibrium describes the steady-state conditions (as defined above) of very-low-density and optically thin plasmas. In this thermodynamic regime, radiative processes and three-body recombination have very low rates, the dominant processes being those which involve two particles, such as the collisional ionization and dielectronic and radiative recombination. The CSD is obtained by equating the rates of those processes [15]. In CE, both the cooling rate and the average ionization are density independent. The cooling

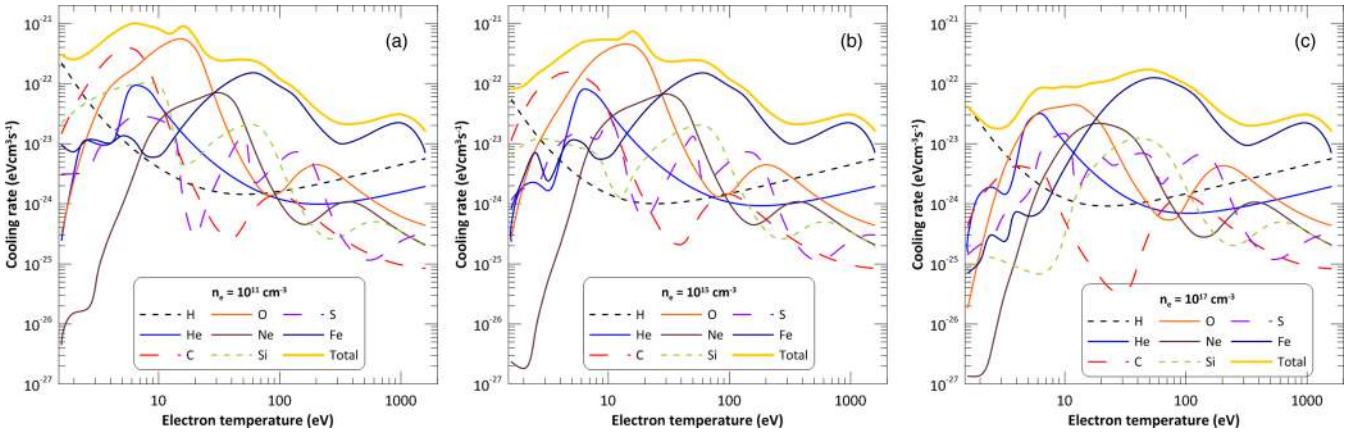

FIG. 2. Contributions of several elements to the mixture cooling rate, as a function of electron temperature and for three electron densities, calculated with MIXKIP. The set of abundances of the elements was extracted from [42]. The total cooling rate (yellow solid line) is the sum of all the elements included in the mixture.

rates in these low-density plasmas play a fundamental role in the radiation hydrodynamics simulations and for this reason there are many calculations of them in CE, such as those cited in Sec. I. Furthermore, their temperature dependence of this quantity rules the onset of thermal instabilities in radiative shocks [70,71], which could be responsible for the origin of several astrophysical objects. On the other hand, the steady-state assumption in the CE approach is no longer valid in astrophysical objects in which the ionization or recombination timescales are longer than the cooling time [1], for example, the stellar coronal loops [3]. In this case, a time-dependent model must be used to obtain the plasma level populations since CE calculations would predict an underionized plasma and then higher cooling rates. However, time-dependent NLTE simulations are not easily implemented in two- or three-dimensional hydrodynamic simulations and CE calculations are still used.

In this section, we analyze the departures from CE of the cooling rates as a function of the plasma conditions and we also compare our results at low density with other simulations carried out assuming CE. First, we analyze the contribution of the different chemical elements to the cooling rate of the mixture as a function of the electron temperature and density, using the solarlike abundances provided by [42]. In Fig. 2 we have represented the contributions of several of them for three electron densities and the cooling rate of the whole mixture. We observe that, for temperatures lower than 30 eV and electron densities of 10^{11} and 10^{15} cm^{-3}, H, He, C, and O are the elements with a larger contribution and, in particular, for temperatures greater than 3 eV the most relevant contributions are due to C and O. For the density of 10^{17} cm^{-3}, we detect that the cooling rate experiences a decrease, fundamentally, in the range of temperature less than 50 eV. The increase in the plasma recombination with the density affects the low-temperature regime more and this fact could explain the decrease of the cooling rate. For electron temperatures higher than 50 eV, the most significant contribution is due to iron and, for an electron density of 10^{17} cm^{-3}, its relevance extends to temperatures higher than 30 eV.

As shown in Fig. 2, oxygen and iron are the main contributors to the cooling rate of the plasma mixture for different ranges of electron temperatures. For this reason, we have also analyzed these two elements. Figure 3 presents a comparison of the cooling rates for plasmas of oxygen, silicon, and iron. Comparisons with CE calculations are made at three electron densities 10^{11}, 10^{15}, and 10^{17} cm^{-3}. In particular, we compare our calculations with those carried out by Schure *et al.* [1], developed to simulate the circumstellar medium of a massive star. They used the SPEX package [72] to obtain a cooling curve including a complete description of line emission which led to cooling rates higher than those provided by other widely used cooling curves [1]. We also compared our calculations with numerical fittings of the cooling rates obtained from Post *et al.* [10] based on an average-atom model to obtain the atomic properties and the rate coefficients of the relevant processes in CE. Cooling rates extracted from Ref. [5] have also been included in the comparison. Finally, for the iron case, a comparison with a NLTE code, FLYCHK [73], is made for an electron density of 10^{11} cm^{-3}. FLYCHK solves rate equations of a collisional-radiative model for the calculation of level population distributions and employs the jj-configuration averaged atomic states and oscillator strengths calculated using the Dirac-Hartree-Slater model, scaled hydrogenic cross sections, and read-in tables.

From Fig. 3(a) we detect good agreement between MIXKIP and the Post *et al.* results for oxygen in the whole range of electron temperatures. The agreement among all the models becomes better for electron temperatures higher than 20 eV, where the average ionization is greater than 4.5 and then the atomic structure of the most abundant ions is simpler. The figure also shows that the cooling coefficients provided by MIXKIP at 10^{11} and 10^{15} cm^{-3} are quite similar for all the temperatures, which means that CE would be accurate for oxygen plasmas for electron densities up to 10^{15} cm^{-3}. According to Fig. 2, at these two densities, oxygen is the most important contributor to the mixture for temperatures from 6 to 30 eV and therefore that result will also apply for the whole mixture. For a density of 10^{17} cm^{-3} we observe that the cooling rates converge to those obtained at lower densities for temperatures higher than 100 eV since the increase of the temperature encourages the CE regime. This result agrees with Griem's criterion [48], which predicts that the plasma

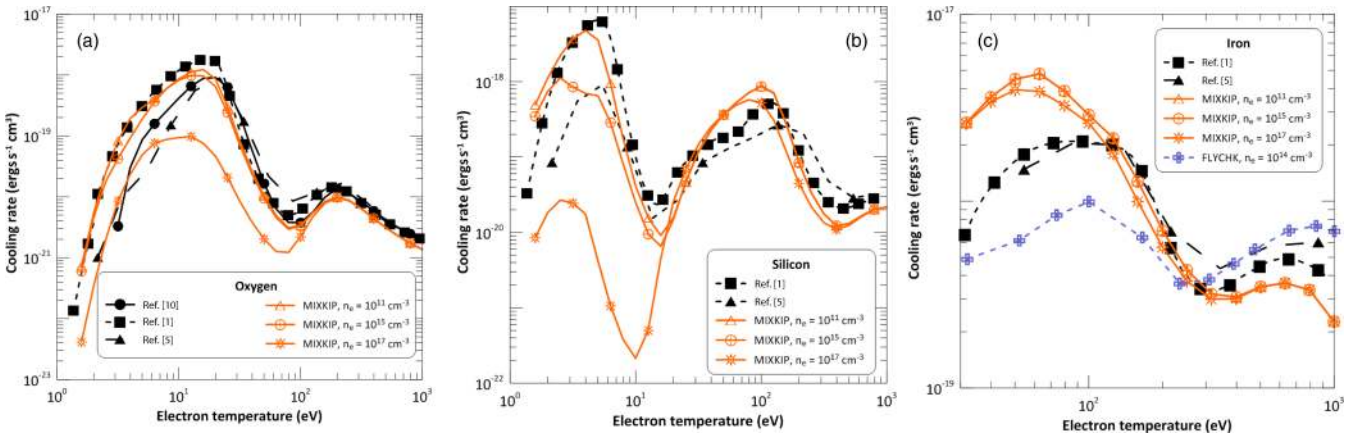

FIG. 3. Cooling rates for oxygen, silicon, and iron, at three electron densities, as a function of the electron temperature. Comparisons with CE calculations [1,5,10] and, for the iron case, with the NLTE FLYCHK code [73] are shown.

should be coronal at this density for electron temperatures higher than around 113 eV.

With respect to silicon, conclusions similar to those for oxygen are obtained, but in this case the disagreements between the cooling rates obtained with MIXKIP at the highest density and at the other two lower ones decrease for temperatures higher than 20 eV, as Fig. 3(b) shows. Figure 3(c) displays the comparison for iron plasmas. In the figure, we have represented the range of temperatures where the contribution of this element to the mixture is more relevant at these densities, according to Fig. 2. For that range of temperatures, we detect that the cooling rates obtained at the three densities are quite similar and therefore the CE assumption would be accurate for these densities. This result will remain for the cooling rate of the whole plasma mixture. On the other hand, the agreement between the models is worse than for oxygen and silicon at temperatures lower than 100 eV. The atomic structure of iron is more complicated than for the other two elements. For temperatures lower than 100 eV, for the iron case, the ions involved have between 20 and 13 bound electrons [see Fig. 1(a)] and in that range we observed in Figs. 1(a) and 1(b) that the disagreements between the NLTE codes in the RPLs are of the same order as those we obtain in the comparison between MIXKIP and the CE models. The agreement improves in the range of electron temperatures 100–300 eV, as was the case in the comparison between the NLTE codes. As previously mentioned, Ne-like Fe is the most relevant ion in that range, with a closed-shell atomic structure, which is simpler than open-shell structures. For higher temperatures the disagreement rises again since open-shell ions are the most abundant. We also detect noticeable differences with FLYCHK results, although this is expected since this code is best suited to intermediate densities out of CE [73].

In Fig. 4 we present a comparison of the cooling rates of the plasma mixture with several calculations of CE models, in particular, with those provided by Schure *et al.* [1], which included 15 elements in their simulations, H, He, C-O, Ne-Si, Ca, Sr, Fe, and Ni. Solar abundances were assumed using those given in Ref. [41]. We have also compared our calculations with the data from Gnat and Sternberg [8]. The authors considered the following elements in the mixture: H, He, C-O, Ne, Mg, Si, S, and Fe. For the elemental abundances of C, N, O, Mg, Si, and Fe we used those reported by Asplund *et al.* [74] for the photosphere of the sun, and for Ne they adopted the enhanced abundances recommended by Drake and Tesla [75]. We have also compared our calculations with the cooling rates extracted from the work of Summers and McWhirter [5] for a mixture of H, He, C-O, Ne-S, Ar-Ca, and V-Cu that used the coronal fractional abundances reported by Withbroe [76]. In MIXKIP, for these comparisons, we have employed the same abundances as in [1]. Figure 4 shows good agreement among all the simulations for electron temperatures higher than 50 eV, although the cooling rates provided by Summers and McWhirter present more differences with respect to the other models. For the range of temperatures 2–20 eV, we detect similarities between the cooling rates of MIXKIP calculations at 10^{14} cm^{-3} and those from Schure *et al.* as well as between the simulations of Gnat and Sternberg and those of Summers and McWhirter. The abundances used in

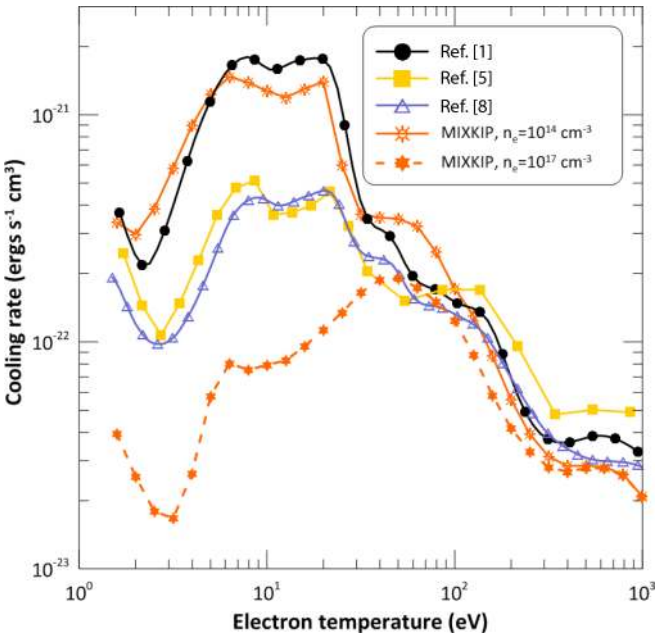

FIG. 4. Comparison of the cooling rates of the plasma mixture, at two electron densities, with calculations of CE models [1,5,8].

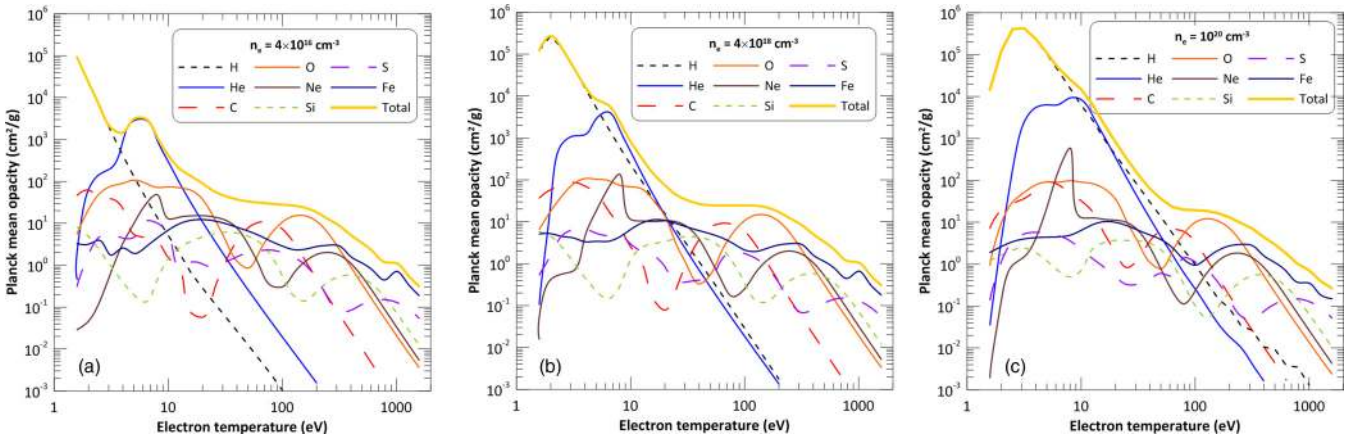

FIG. 5. Contributions of several elements to the mixture Planck mean opacity, as a function of electron temperature and for three electron densities, calculated with MIXKIP. The set of abundances of the elements was extracted from [42]. The total Planck mean (yellow solid line) is the sum of all the elements included in the mixture.

MIXKIP and by Schure *et al.* are different from those used in the other two models, but this fact cannot explain the appreciable differences observed. In that range of temperatures, elements such as O and Si contribute significantly to the cooling rate of the mixture. As shown in Figs. 3(a) and 3(b), MIXKIP and Schure *et al.* provided quite similar results for the cooling rates of these two elements in this range of temperatures, whereas the values extracted from the work of Summers and McWhirter presented noticeable differences. Therefore, we can conclude that the discrepancies in the cooling rates of the mixture are mostly due to differences in the atomic structures and processes considered in the models.

With respect to the calculations with MIXKIP at electron densities of 10^{14} and 10^{17} cm^{-3}, we detect similarities for the cooling rates for temperatures higher than 100 eV, whereas for lower temperatures the differences can reach one order of magnitude. These discrepancies, which were expected according to the results already obtained for oxygen and iron, are considerably larger than those obtained among all the CE models, indicating that CE is not reached for temperatures lower than 100 eV at 10^{17} cm^{-3} and NLTE simulations would be necessary.

C. Departures from local thermodynamic equilibrium

Local thermodynamic equilibrium is reached in plasmas whose dimensions are significantly smaller than the mean free path of the photons emitted from the plasma but are much longer than the collision length of the electrons and the ions. Local thermodynamic equilibrium conditions develop when the rates of the collisional processes and their inverse are equal and therefore LTE conditions can be attained only at high densities. In this thermodynamic regime, the ion abundances in MIXKIP are obtained through the Saha equation

$$\frac{N_{\zeta+1}n_e}{N_\zeta} = \frac{Z_e Z_{\zeta+1}}{Z_\zeta} e^{-(I_\zeta - \Delta I_\zeta)/kT_e}, \tag{30}$$

where Z_e and Z_ζ are the partition functions of free electrons and ions ζ, respectively, I_ζ is the ionization potential of the ionization stage ζ, and ΔI_ζ is the CL of the ionization potential due to the plasma environment. The atomic plasma level populations are then obtained assuming a Boltzmann distribution.

In this section, we have analyze the departures from LTE of the Planck and Rosseland mean opacities, as a function of the plasma conditions, and we also compare our results with other simulations carried out assuming LTE. First, we analyze the contribution of the different chemical elements to the Planck mean opacity of the mixture as a function of the electron temperature and density, using the solarlike abundances provided by [42]. In Fig. 5 we represent the contributions of several of them for three electron densities and the Planck mean opacity of the whole mixture. We detect that the Planck mean opacity is mainly ruled by H and He in the low-temperature regime (temperatures lower than 10 eV) for the two lowest densities represented. At 10^{20} cm^{-3}, the increase of the plasma recombination leads to an extension of their importance up to temperatures around 60 eV. Another two relevant contributors to the mean opacity are O and Fe. The former presents a significant contribution for temperatures from 100 to 300 eV for the three densities represented and around 20 eV for the two lowest densities. Iron contributes most to the range of electron temperatures higher than 300 eV. Due to their importance, as in the preceding section, we also carry out an analysis of the departures from LTE of mean opacities of oxygen and iron and, for the latter, we compare our simulations with LTE calculations.

In Fig. 6 we present a comparison, as a function of the electron temperature and at four mass densities, of the average ionization and Planck and Rosseland mean opacities of oxygen, calculated with MIXKIP, in both LTE and NLTE, and the ATOMIC code [23] in LTE. With respect to the average ionization, MIXKIP LTE and ATOMIC provide close results for temperatures higher than 10 eV, with relative differences generally lower than 5%. For temperatures equal to or less than 10 eV, these differences become greater. This behavior may be attributed to two factors. The first one is the different atomic description used in each code: a DLA single configuration in intermediate coupling in ATOMIC [77] and DCA in MIXKIP. It has been shown that the discrepancies between DLA and DCA descriptions increase as the temperature decreases. The second factor is related to the modeling of the effect of the plasma

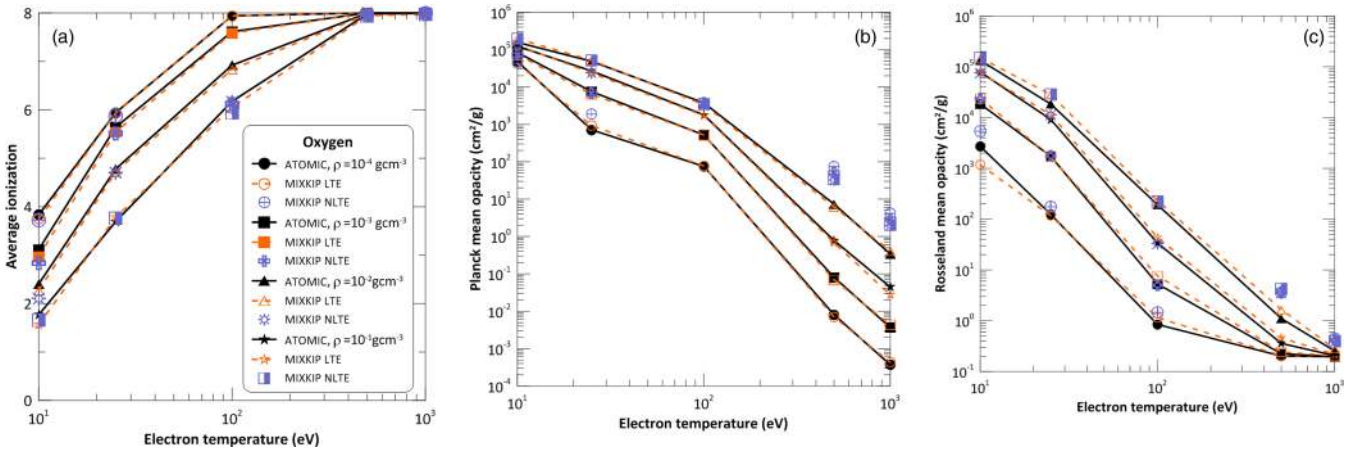

FIG. 6. Comparison of (a) average ionization and (b) Planck and (c) Rosseland mean opacities with ATOMIC [23] simulations in LTE for oxygen.

environment in the atomic kinetics calculations. For a fixed density, the decrease of the temperature enhances the plasma effect and therefore, in this range of lower temperature, the calculations are more sensitive to the model used to describe that effect. In the equation of state used in ATOMIC for the calculation of the ion abundances, the plasma effect is taken into account by means of hard-sphere occupation probability terms [78]. On the other hand, as previously mentioned, the plasma influence in MIXKIP is included through the Stewart-Pyatt (SP) model for the CL. The SP model converges to the ion-sphere (IS) model when the coupling parameter [79], which represents (for plasmas obeying classical statistics) the ratio of the average Coulomb and kinetic energies, is much larger than unity. For the mass densities represented and electron temperatures equal to or lower than 10 eV, that parameter ranges from 0.15 to 0.30 and therefore the SP model does not converge to the IS one. In this range of temperatures we have also performed calculations using an IS based model proposed by Crowley [80] instead of the SP model, obtaining results closer to those of ATOMIC simulations than those obtained using the SP model, which seems to confirm our assumption.

With respect to LTE and NLTE simulations of the average ionization, Fig. 6 shows that they are close for the whole range of temperatures only for a mass density of 0.1 $\mathrm{g\,cm^{-3}}$ (electron densities range from 6×10^{21} to 3×10^{22} $\mathrm{cm^{-3}}$), with relative differences not exceeding 5%. For the other mass densities, only for temperatures lower than 25 eV NLTE and LTE results are close, with relative differences around 5% or lower. As the temperature increases, the departure from the LTE regime becomes larger and at 100 eV noticeable differences between the average ionizations provided by both simulations are already detected for the three lower densities considered. At this temperature and for all mass densities, the NLTE model predicts an average ionization around 6 (He-like ion). The average ionizations obtained in the LTE regime are more sensitive to the density and they are overestimated with regard to the NLTE calculations, predicting for the lowest density, for example, that the fully stripped ion is the most probable at 100 eV. At this temperature and density (around an electron density of 10^{19} $\mathrm{cm^{-3}}$), the contribution of oxygen to the mean opacities of the mixture is large, as shown in Fig. 5(c), and can lead to appreciable changes. Furthermore, the NLTE simulations show a plateau in the average ionization associated with the He-like ion for electron temperatures ranging from 20 to 100 eV, which is not observed in LTE. We also detect that both the LTE and NLTE simulations predict the fully stripped ion as the most abundant for electron temperatures greater than 300 eV. However, despite this agreement, the plasma is in NLTE and there are noticeable differences in the mean opacities, as we will show.

Figures 6(b) and 6(c) show general agreement between MIXKIP LTE and ATOMIC for the Planck and Rosseland mean opacities within 20% and 30%, respectively, these discrepancies being associated with the different atomic descriptions used in the calculation of the atomic spectra. In ATOMIC, a DLA approach is employed, although for the bound-bound opacity of elements beyond Si a combination of DLA and mixed-UTA approaches is used [23]. In MIXKIP a DCA-UTA approach is used. The agreement is worse for the Rosseland mean opacity. This property is more sensitive to the line shape than the Planck opacity and in the UTA formalism the detailed line spectra of the DLA descriptions are replaced by Gaussian distributions. Figure 6(c) shows that for the case of lowest density and temperature, where the Doppler and collisional broadenings are small and then the lines are narrower, the disagreement between MIXKIP and ATOMIC Rosseland mean opacities increases considerably, which corroborates our statement.

The differences between LTE and NLTE opacities present a similar behavior with density and temperature to the average ionizations. However, the differences for the former properties are larger than for the latter, which indicates that the mean opacities are more sensitive to the thermodynamic regime than the average ionizations. With respect to the Rosseland mean opacities, for the greatest density (10^{-1} $\mathrm{g\,cm^{-3}}$) at low temperatures the discrepancies are less than 5%. As expected, the disagreement increases with the temperature and, for example, at a temperature of 500 eV ($n_e = 3 \times 10^{22}$ $\mathrm{cm^{-3}}$), where oxygen still has a non-negligible contribution to the mixture, it reaches 155%, which is considerably larger than the one between both LTE simulations, which is around 30%. The disagreement with respect to LTE simulations also becomes

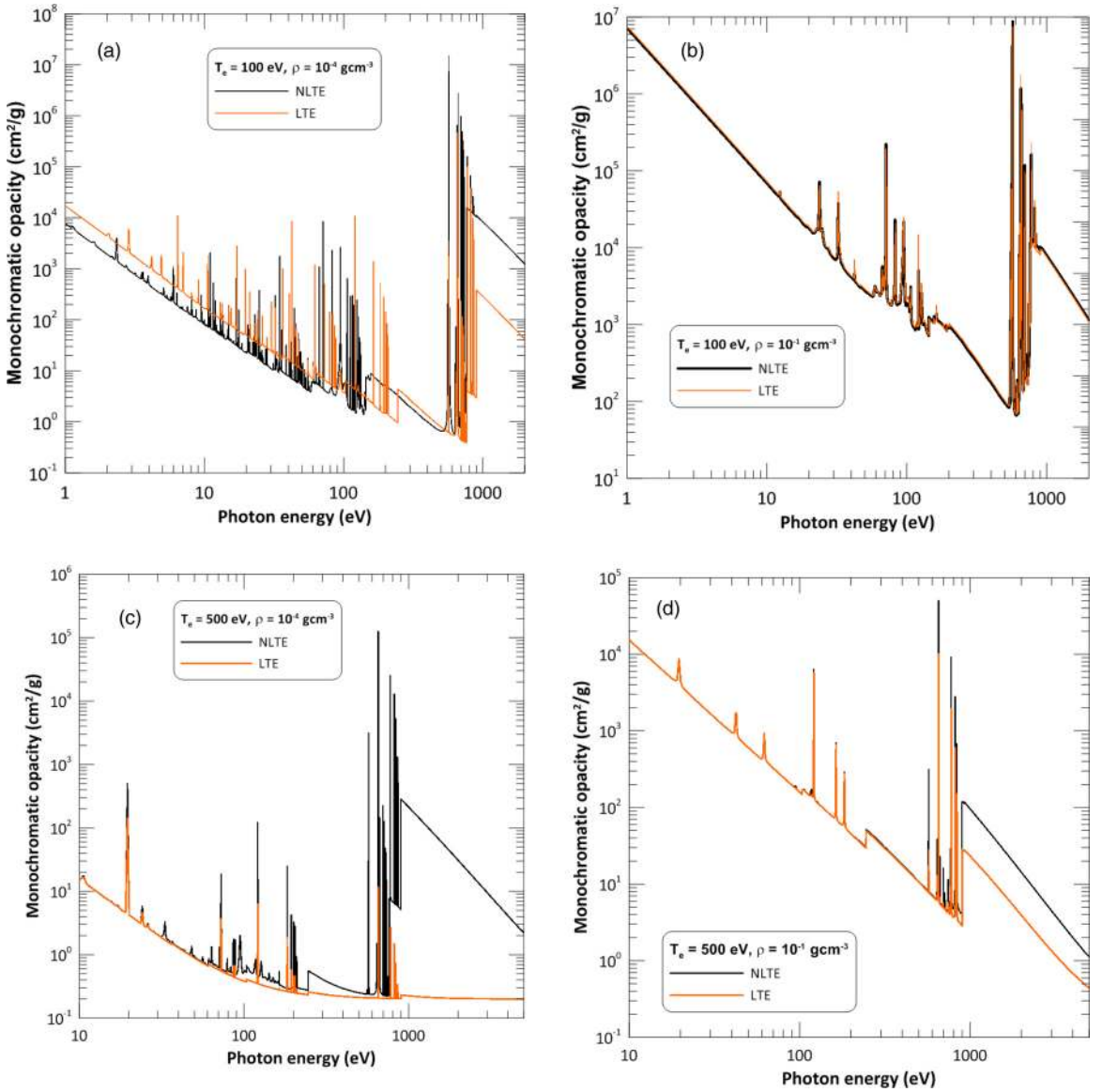

FIG. 7. Comparison of monochromatic opacities of oxygen plasmas obtained assuming LTE and NLTE regimes for a fixed electron temperature and two mass densities.

greater as the density decreases and, at that temperature, the relative differences are around 1700% for a mass density of 10^{-4} g cm^{-3} ($n_e = 3 \times 10^{19}$ cm^{-3}) and 1400% for a mass density of 10^{-3} g cm^{-3} ($n_e = 3 \times 10^{20}$ cm^{-3}). These differences are considerable larger than those obtained from the comparisons between both LTE models, which are around 22% and 8%, respectively. At a temperature of 500 eV, NLTE Rosseland mean opacities are almost density independent, as shown in Fig. 6(c). We have represented in Figs. 7(c) and 7(d) the monochromatic opacities for these temperatures and for the lowest and highest mass densities. The weighting function for the Rosseland mean peaks at $3.8T_e$ (eV), i.e., at a photon energy of 1900 eV for this temperature. Therefore, the largest contribution is due to the photoionization of the $1s$ H-like ion and since the abundances of this ion are quite similar at both densities (0.53×10^{-1} and 0.66×10^{-1} at mass densities 10^{-4} and 10^{-1} g cm^{-3}, respectively), the values of the NLTE mean opacities are close. On the other hand, the LTE simulation is more sensitive to the changes in density, as shown in Figs. 7(a) and 7(b), since the abundances of the H-like ion disagree by two orders of magnitude at these two densities. Figures 7(c) and 7(d) represent the monochromatic opacities for these two mass densities at an electron temperature of 100 eV. In this case, the weighting function peaks at a photon energy of 380 eV and the depths of the transmission windows in this region of photon energies are quite similar in the LTE and NLTE calculations, which explains the similarities found between the Rosseland mean opacities at this temperature.

Larger differences are detected for the LTE and NLTE Planck mean opacities, as shown in Fig. 6(b). The discrepancies are already noticeable for the two lower densities for electron temperatures greater than 100 eV. The weighting function in this case peaks at $2.8T_e$ (eV), i.e., at a photon energy of 280 eV for an electron temperature of 100 eV. The Planck opacity is mainly determined by the strength of the absorption peaks. This mean opacity is mainly ruled by

the absorption structure located around the photon energy range from 400 to 800 eV [see Figs. 7(a) and 7(b)], which is mainly due to the line transitions of He- and H-like ions. The similarity between the strengths of the mean peaks in the structure for the two mass densities in NLTE simulations explains why their Planck mean opacities are very close. On the other hand, the lesser abundances predict by the LTE simulation for the He- and H-like ions at 10^{-1} g cm^{-3} explain the large discrepancies obtained for both the monochromatic and Planck mean opacities. As expected, the agreement becomes better as the mass density increases, as shown in Fig. 7(b). The disagreement between LTE and NLTE Planck mean opacities increases with temperature and, at electron temperatures of 500 and 1000 eV and the greatest mass density, the relative differences are around 350%. These differences becomes even larger as the mass density decreases and they can reach three orders of magnitude at a density of 10^{-4} g cm^{-3}. For example, at 500 eV, the weighting function of the mean opacity reaches its maximum at a photon energy of 1400 eV. The great differences observed in the line transitions and in the photoionization of the $1s$ level H-like ion in the monochromatic opacities represented in Figs. 7(c) and 7(d) help to explain these results.

We have made comparisons in LTE with OP opacities [17] and a DLA model with state mixing within one electron configuration presented in [28] for iron, which is also an element with a large contribution to the opacity of the mixture. In particular, we have made an isothermal and isodensity study of the Rosseland and Planck mean opacities. Good agreement is observed in general between the OP and the DLA model at a temperature of 19.3 eV for mass densities up to around 10^{-3} and 10^{-4} g cm^{-3} for Planck and Rosseland mean opacities, respectively [see Fig. 8(a)]. The discrepancies between the models increase with the mass density. According to [28], these differences may be attributed to the model of the equation of state used in each code to calculate the populations in LTE. At this relatively low temperature and high densities (near electron densities of 10^{22} cm^{-3}) the effect of cutting levels in the partition function can be significant. In the calculation made in [28], the model used is based on the model of Stewart and Pyatt. On the other hand, the OP uses an occupation probability formalism for the truncation of internal partition functions [78]. With respect to the small differences between both models at low densities, they may be associated with the different atomic description employed and to the set of atomic levels included. The MIXKIP LTE provides results that in general show good agreement with those obtained with the DLA model, with maximum relative differences around 15% and 25% for the Planck and Rosseland mean opacities, respectively. These differences are mainly due to the different atomic description used in each calculation. For this reason, the relative differences in the mean opacities between both models decrease as the density increases. As mentioned above, the model used in MIXKIP to include the effect of plasma environment is based on the Stewart-Pyatt model and, for this reason, the mean opacities at high densities are more similar to those obtained with the DLA model than those provided by the OP.

Figure 8(a) shows that NLTE and LTE Planck mean opacities are noticeably different for mass densities up to

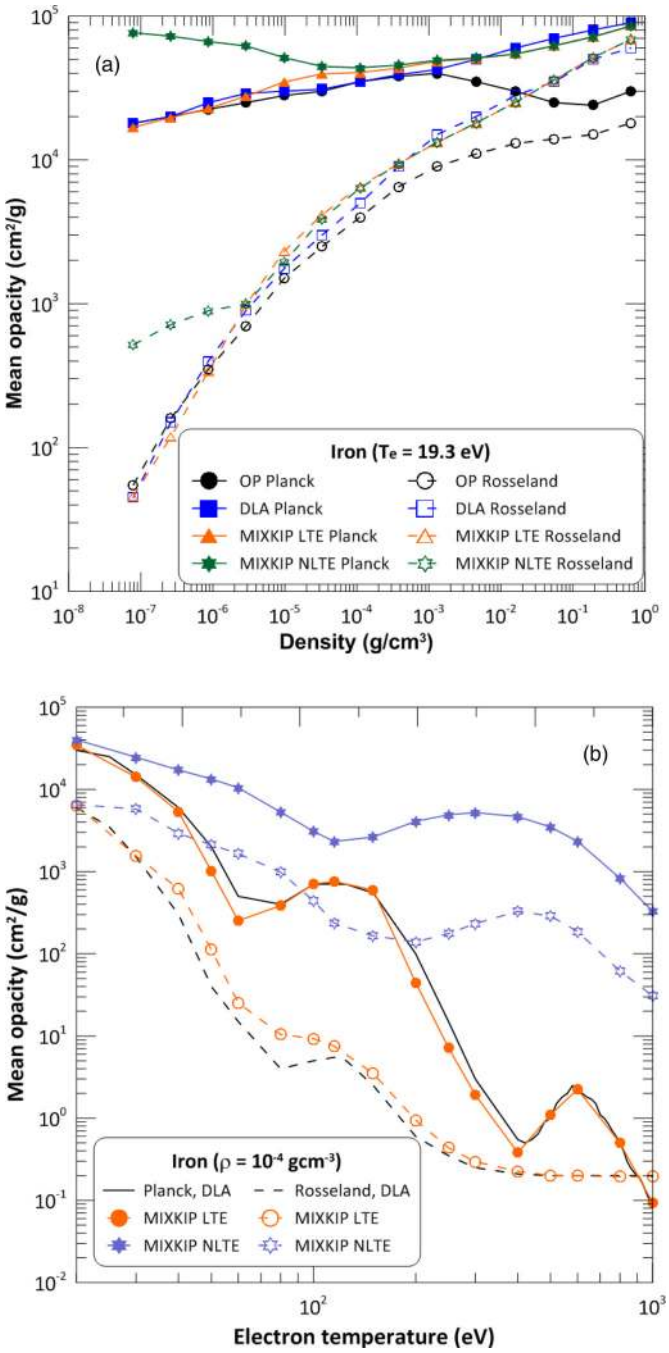

FIG. 8. Comparison of MIXKIP LTE and NLTE mean opacities: (a) isothermal analysis at 19.3 eV, showing a comparison with the OP [17] and a DLA simulation [28], and (b) isodensity analysis at 10^{-4} g cm^{-3}, showing a comparison with a DLA simulation [28].

10^{-6} g cm^{-3} ($n_e \sim 10^{17}$ cm^{-3}) with relative differences always larger than 100%, reaching relative differences as much as 350% for the lower densities. These differences are significantly larger than those obtained between the LTE models (around 15%). For mass densities higher than 3.3×10^{-5} g cm^{-3} ($n_e \sim 3.1 \times 10^{18}$ cm^{-3}), the relative differences are less than 10%, falling below 1% for mass densities higher than 5×10^{-3} g cm^{-3} ($n_e \sim 3.2 \times 10^{20}$ cm^{-3}). With respect to the Rosseland mean opacities, for the two lower mass

densities, the relative differences reach the 1000% and 500%, respectively, which are considerably higher than those obtained between the LTE models (around 20%). The disagreement diminishes as the density increases, dropping below the 20% and 1% for mass densities greater than 10^{-5} ($n_e = 10^{18}$ cm^{-3}) and 4×10^{-4} ($n_e = 3.3 \times 10^{19}$ cm^{-3}) g cm^{-3}, respectively. Therefore, at this temperature, the plasma could be assumed to be in the LTE regime for mass densities greater than 5×10^{-3} g cm^{-3}.

The analysis of the mean opacities as a function of the temperature (10–1000 eV) for a fixed mass density (10^{-4} g cm^{-3}) is presented in Fig. 8(b). For this range of temperature, the electron density is between 8.1×10^{18} and 2.8×10^{19} cm^{-3}. We detect general agreement between the MIXKIP LTE and the DLA model of [28]. The differences may be attributed, as in the case of the isothermal analysis, to differences in the atomic description and the atomic configurations selected in each model. We observe in the figure that the relevance of the differences begins to drop for electron temperatures higher than 300 eV, which is the range of temperatures in which iron contributes most to the mixture. For a fixed mass density, the electron density increases with the temperature. At high temperatures, Doppler and collisional broadenings become more relevant and then the overlapping of the line transitions. As a consequence, the differences between DCA-UTA and DLA models decrease [77]. With respect to NLTE calculations, the differences become noticeable for temperatures higher than 50 eV, reaching almost two orders of magnitude. They increase with the temperature, achieving three and four orders of magnitude for the Planck and Rosseland mean opacities, respectively, at 1000 eV. Since iron is the most relevant contributor to the opacities of the mixture in that range of high temperatures, as shown in Fig. 5, this will produce noticeable changes in these properties. The origin of these wide discrepancies at high temperatures is the different average ionizations predicted by LTE and NLTE simulations which result in quite different monochromatic opacities, as Figs. 9(a) and 9(b) adequately illustrate. At 100 eV, the average ionizations obtained from LTE and NLTE calculations are 14.9 and 17.6, respectively, the most relevant ions being Fe^{14+}-Fe^{16+} and Fe^{17+}-Fe^{18+}, respectively. Therefore, monochromatic opacities differ in the strength of the peaks and the depth of the valleys and particularly where the weighting functions of the Planck and Rosseland mean opacities reach their maximum, at photon energies of 280 and 380 eV, respectively [see Fig. 9(a)]. Figure 9(b) shows that the difference is more drastic at 500 eV, where the LTE and NLTE average ionizations are 24.1 and 17.5, respectively, and the most abundant ions are Fe^{23+}-Fe^{26+} and Fe^{16+}-Fe^{19+}, respectively. In this case, the LTE spectrum is considerably shifted to higher energies. As a consequence, its contribution at photon energies 1400 and 1900 eV (where the weighting functions peak for Planck and Rosseland means, respectively), is considerably smaller than the NLTE absorption spectrum.

Finally, in Figs. 10(a) and 10(b) we present a comparison of the Rosseland and Planck mean opacities for the plasma mixture calculated in LTE and NLTE with those obtained using ATOMIC in LTE. For the calculation, in both the MIXKIP and ATOMIC codes we use the same chemical elements already mentioned in Sec. II for the plasma mixture and for

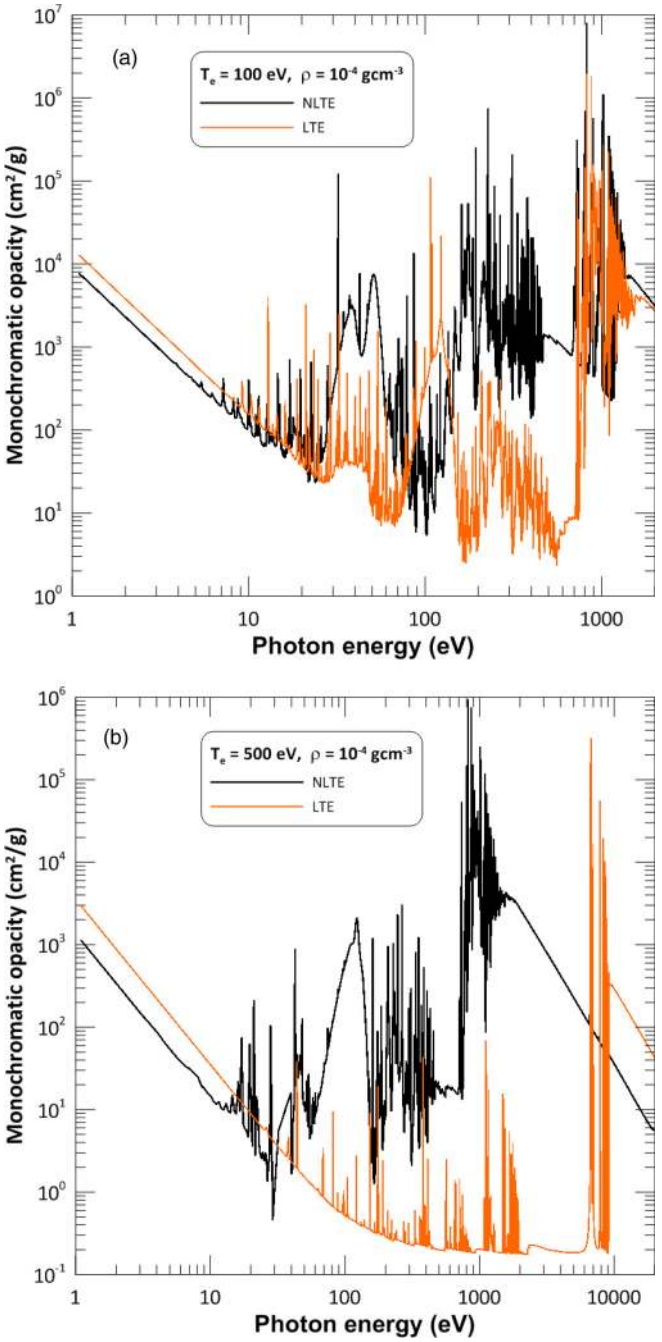

FIG. 9. Comparison of monochromatic opacities of iron plasmas obtained assuming LTE and NLTE regimes for a fixed mass density and two electron temperatures.

their abundances those presented in Ref. [42]. The MIXKIP LTE and ATOMIC mean opacities present similar behavior for density and temperature. The differences detected may be attributed to two factors, the different atomic descriptions considered in both models and the set of configurations included, since the latter is more complete in ATOMIC, for the elements of the mixture, than the one used in the present work.

These two factors cause relative differences for the Rosseland mean opacity at low temperatures and for the lowest density represented around 80%, which are reduced to around

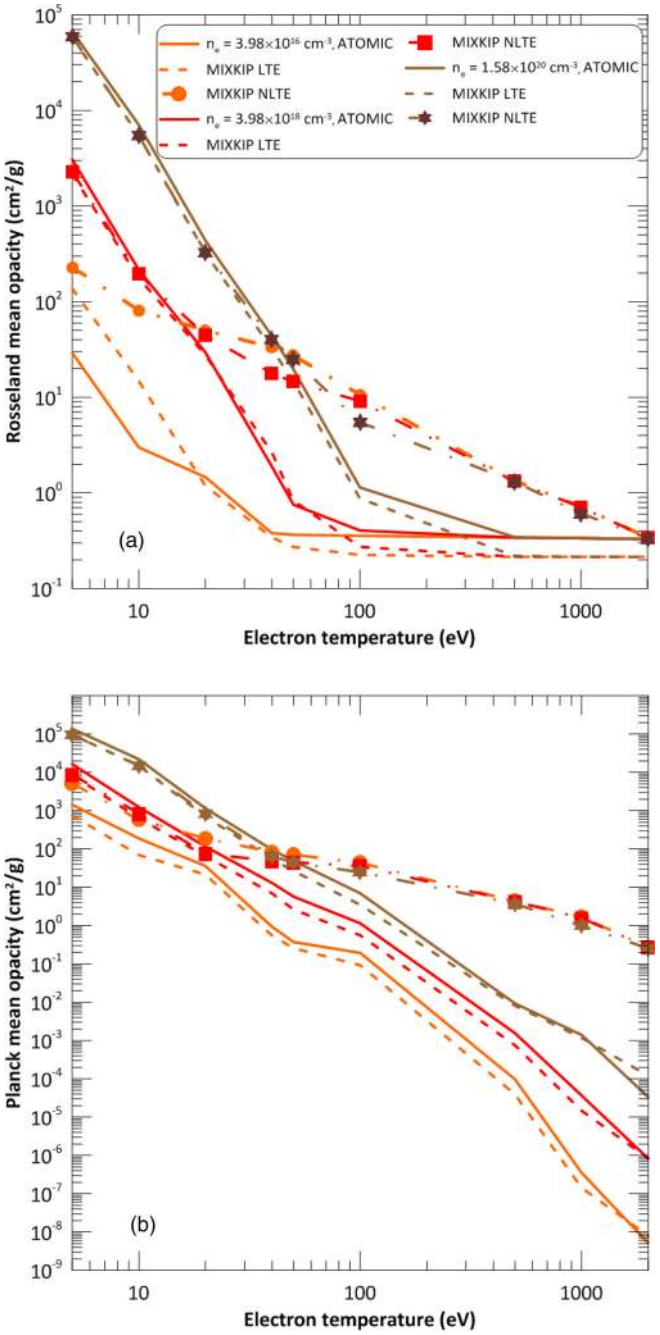

FIG. 10. Comparison of Rosseland and Planck mean opacities calculated with MIXKIP in LTE and NLTE regimes with those obtained using the ATOMIC code [23] in LTE.

30% and 20% for the intermediate and the highest densities shown, respectively. As the temperature increases the relative differences decrease, to around 35% for the lowest density and less than 20% for the other two densities. As the temperature increases, we detect that the Rosseland mean opacities tend to have a constant value, which is due to the scattering contribution to the opacity. For the lowest density represented, this behavior is reached at temperatures around 40–50 eV. At these temperatures, the elements with a greater contribution to the opacity (carbon and oxygen, mainly) are fully ionized for this electron density in LTE simulations. The increase of the recombination with the density causes the temperature in which the constant behavior begins to shift to higher values, around 300 and 600 eV, respectively, for the other two densities represented. At these electron temperatures and densities the LTE model predicts that all the elements in the mixture are fully striped. In MIXKIP, the Thomson formula is used to model the scattering, whereas in ATOMIC, a more elaborate method is employed [23], which is the reason for the disagreement in the constant value of the Rosseland opacities between both models [see Fig. 10(a)]. This behavior is not obtained in NLTE since the average ionization predicted for these densities and temperatures is lower than in LTE simulations and then the scattering contribution to the opacity is not relevant. For the highest density, the relative differences between LTE and NLTE simulations are lower than 50% for electron temperatures up to 50 eV. Then the discrepancies increase with temperature, reaching the 800% at an electron temperature of 500 eV (where the disagreement between both LTE calculations is around 50%) and decreasing to 200% at a temperature of 1000 eV. As expected, the disagreement increases as the density decreases and for the lowest density represented the discrepancies reach 5000% at a temperature of 100 eV, whereas the relative difference between the MIXKIP LTE and ATOMIC is around 50%.

With respect to the Planck mean opacities, the relative differences between the MIXKIP LTE and ATOMIC are, in general, lower than 60% and 45% for the lowest and the highest densities represented, respectively. As the density increases, the differences between detailed and statistical atomic descriptions are reduced. Figure 10(b) shows the great discrepancies obtained between the LTE and NLTE simulations for electron temperatures higher than 20 eV. As mentioned before, the Planck mean opacities mainly depend on the strength of the peaks in the absorption spectra and they are related to the plasma charge-state distribution, which is noticeably different for the plasma conditions represented. This fact explains these great discrepancies that can reach several orders of magnitude. Both NLTE Rosseland and Planck mean opacities are less sensitive than LTE ones to changes in density in the range of plasma conditions represented.

TABLE III. Comparison of the average ionizations of oxygen from LTE and NLTE optically thin and thick models at two electron temperatures, three mass densities, and three plasma slab widths.

		n_e (cm^{-3})		
T_e (eV)	Model	10^{17}	10^{18}	10^{19}
10	NLTE	3.97	4.04	3.81
10	NLTE d_1	4.93	4.59	3.87
10	NLTE d_2	5.16	4.59	3.87
10	NLTE d_3	5.16	4.59	3.87
10	LTE	5.28	4.59	3.87
100	NLTE	6.04	6.05	6.06
100	NLTE d_1	6.13	6.72	6.92
100	NLTE d_2	6.80	6.96	6.97
100	NLTE d_3	6.97	6.97	6.97
100	LTE	8.00	8.00	8.00

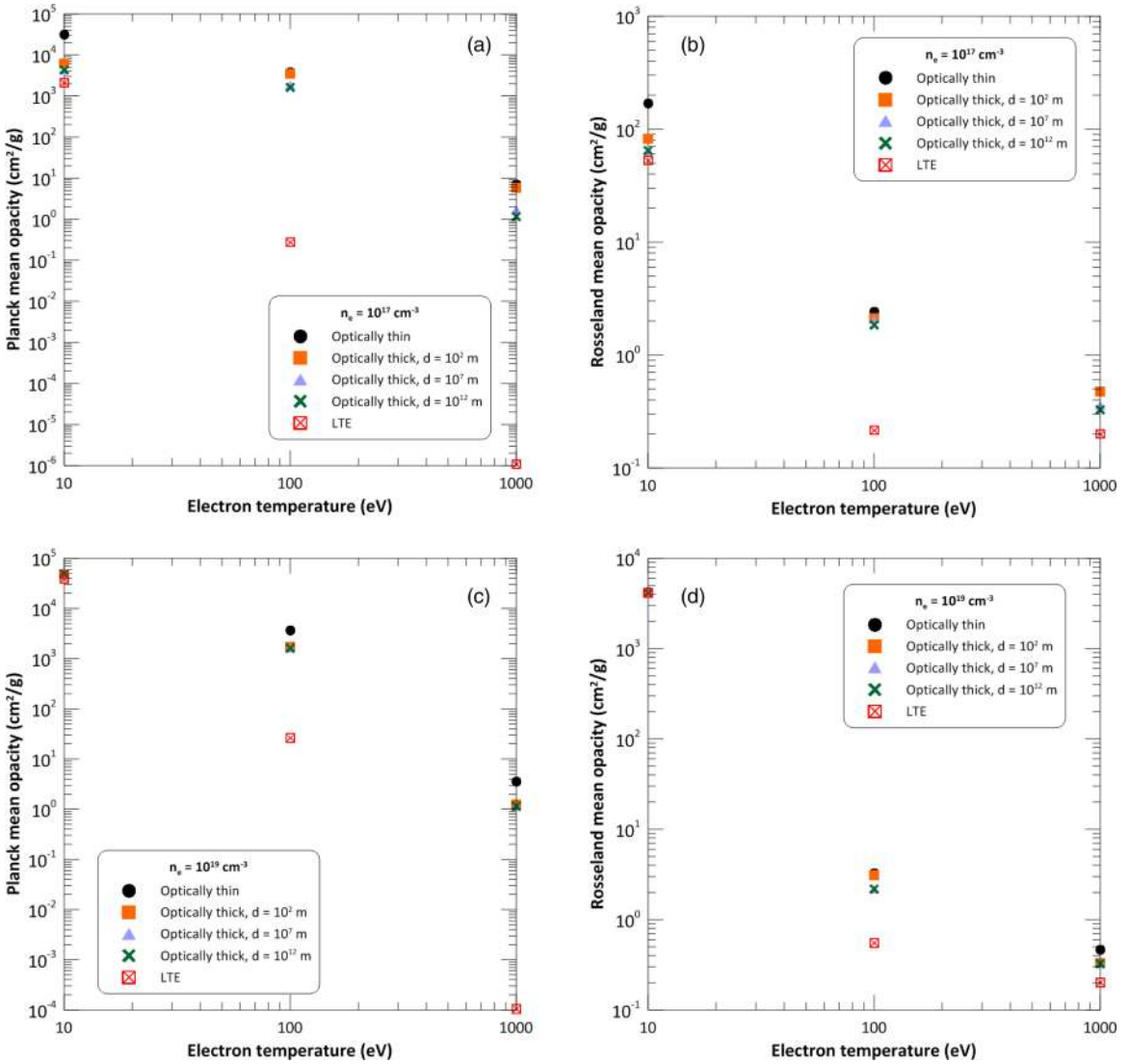

FIG. 11. Comparison of Planck and Rosseland mean opacities of oxygen plasmas obtained from LTE and NLTE optically thin and thick models at three temperatures and for three plasma slab widths.

D. Influence of the plasma self-absorption

The analysis carried out in the preceding section was done by assuming the plasma to be optically thin. However, due to the dimensions of the plasma, it could be the case that the plasma self-absorption becomes relevant and this could modify the results obtained in the optically thin NLTE simulations. In this section, we present a brief analysis of the influence of the opacity effects on the calculation of the plasma radiative properties. As previously mentioned, these effects are included in MIXKIP through the escape factor formalism. For the study, we consider plasmas of oxygen and iron with planar geometry at three electron densities and temperatures, 10^{17}, 10^{18}, and 10^{19} cm^{-3} and 10, 100, and 1000 eV, respectively. For the plasma slab width, three values have been simulated, $d_1 = 10^2$ m, $d_2 = 10^7$ m, and $d_3 = 10^{12}$ m. For fixed plasma conditions, as the optical depth increases with the plasma geometrical dimension, the probability that the photon will be thermalized before it escapes approaches unity [81]. When this happens for any photon frequency the source function eventually thermalize and tends to the Planck function. Therefore, the increase of the plasma width in the optically thick simulations leads to values closer to those of LTE calculations than those obtained in the NLTE optically thin approach.

In Table III we present a comparison for oxygen of the average ionizations obtained in LTE and NLTE optically thin and thick approaches, for those plasma widths and electron densities, and at temperatures of 10 and 100 eV. The plasma self-absorption increases the population in the atomic excited configurations. These may undergo a subsequent ionization due to other atomic processes in the plasma and, as a consequence, the average ionization rises. At 10 eV we detect that for the two highest densities, the average ionizations obtained in the optically thick situation are equal to those provided by the LTE model, even for the smallest plasma width and this could be due to a preponderance of the collisional processes. This result also holds true for the Rosseland and Planck mean opacities, as shown in Figs. 11(c) and 11(d). The opacities decrease with the plasma self-absorption due to the decrease of the population in the ground configurations of the ions.

On the other hand, for the same electron temperature and at a plasma density of 10^{17} cm^{-3}, we observe that the average ionization is the same for the two largest plasma widths and they do not reach the LTE one, although they are close. Figures 11(a) and 11(b) show that the mean opacities tend to the LTE values. We also observe in Table III that the changes in the average ionization, when the plasma self-absorption is included, are greater as the density decreases, which could lead to a relative increase of the relevance of the radiative processes with respect to the collisional ones. For the electron temperature of 100 eV, the changes in the average ionization are lower than at 10 eV and this could be because a closed-shell He-like ion is the most abundant. At this temperature, and for the three densities and plasma widths, the average ionizations converge to the same value, which is between the optically thin and LTE results. With respect to the mean opacities, we detect some slight differences, as shown in Figs. 11(a)–11(d). The ions involved are almost the same in optically thin and thick calculations and the discrepancies fundamentally come from the differences in their abundances. Unlike at electron temperature of 10 eV, in this case the changes in the average ionization are most relevant at higher densities. The relative importance of the collisional processes is lower at 100 eV than at 10 eV and therefore self-absorption effects have an increased effect. We have not listed the average ionizations at 1000 eV because all the models predict the same average ionization since at this temperature the full stripped ion is the most abundant. Figures 11(a) and 11(c) show a decrease of the mean opacities with the plasma length but they are still quite close to the optically thin calculations. In either case, with respect to a solarlike abundance plasma mixture, the contribution of oxygen to the radiative properties of the mixture, for the densities analyzed, is most relevant for electron temperatures from 10 to 300 eV.

In Table IV we present a comparison of the average ionizations for iron calculated with the same models as for oxygen but, in this case, at electron temperatures of 100 and 1000 eV since in this range of temperatures the contribution of iron to the radiative properties of the plasma mixture with solar abundances is more relevant. The behavior of the average ionization for density and the plasma slab width is similar to the oxygen case. However, since the differences between LTE and NLTE values are larger than for oxygen, the average ionizations obtained with optically thick models for iron are not so close to the LTE results.

TABLE IV. Comparison of the average ionizations of iron from LTE and NLTE optically thin and thick models at two electron temperatures, three mass densities, and three plasma slab widths.

		n_e (cm^{-3})		
T_e (eV)	Model	10^{17}	10^{18}	10^{19}
100	NLTE	11.91	13.39	15.98
100	NLTE d_1	13.85	15.79	15.98
100	NLTE d_2	15.69	15.99	16.45
100	NLTE d_3	16.00	16.48	16.63
100	LTE	21.01	19.45	17.97
1000	NLTE	17.94	18.22	19.12
1000	NLTE d_1	18.49	19.79	22.04
1000	NLTE d_2	20.88	23.14	23.94
1000	NLTE d_3	23.59	23.94	23.95
1000	LTE	26.00	26.00	26.00

In Figs. 12(a)–12(d) we present a comparison of the Rosseland and Planck mean opacities at electron densities of 10^{17} and 10^{19} cm^{-3}. As expected, for fixed plasma length and temperature, the effect of the plasma self-absorption increases with the electron density since the optical depth increases as well. The opposite behavior is obtained with the temperature because the plasma absorption decreases. For example, at an electron temperature and density of 100 eV and 10^{19} cm^{-3}, respectively, the Planck and Rosseland mean opacities in the optically thick simulations decrease considerably with respect to the optically thin case and they are very close to the LTE result. On the other hand, there are still noticeable differences between LTE and optically thick situations even for the largest plasma length considered at a temperature of 1000 eV. At an electron density of 10^{17} cm^{-3}, the effect of the plasma self-absorption is not too relevant at both temperatures.

IV. CONCLUSION

Radiation-hydrodynamics simulations usually need radiative properties in wide ranges of plasma conditions. Many of the databases of these properties have been obtained in either CE or LTE approaches due to the complexity of the implementation of NLTE models in the hydrodynamics codes. However, radiative properties are sensitive to the plasma thermodynamic regime and when the plasma is far from the CE or LTE regimes, the disagreement with respect to NLTE simulations can be significant. In the present work, we have carried out NLTE calculations of the radiative properties of an astrophysical plasma mixture for electron temperatures and densities ranging from 1 to 1000 eV and 10^{11} to 10^{20} cm^{-3}, respectively. These simulations have enabled an analysis of departures of from CE and LTE results when the plasma is in NLTE. This study has also been made for iron and oxygen, due to their relevance in these properties of the mixture. The plasma level populations were obtained solving a collisional-radiative model assuming homogeneous plasmas to be in steady state and optically thin. For the free electrons, a Maxwell-Boltzmann energy distribution was assumed. Due to the wide range of plasma conditions analyzed, a statistical atomic description based on the DCA-UTA approach was used in order to achieve a compromise between the accuracy in the atomic description and computational costs. The main objective of this work was not to provide precise values of the radiative properties of the plasma mixture but to illustrate and quantify the effect of NLTE in their simulations. In either case, we have compared our model with other codes, in NLTE, CE, and LTE regimes, and we have obtained that our results reproduce the behaviors predicted by those codes and that the relative differences are generally lower than 50%. These discrepancies are considerably lower than the differences obtained between NLTE, CE, and LTE simulations when the plasma fulfills the criteria of these thermodynamic regimes. We determined the electron densities and temperatures where the departures of the cooling rates and mean opacities from CE and LTE results, respectively, were noticeable. For some

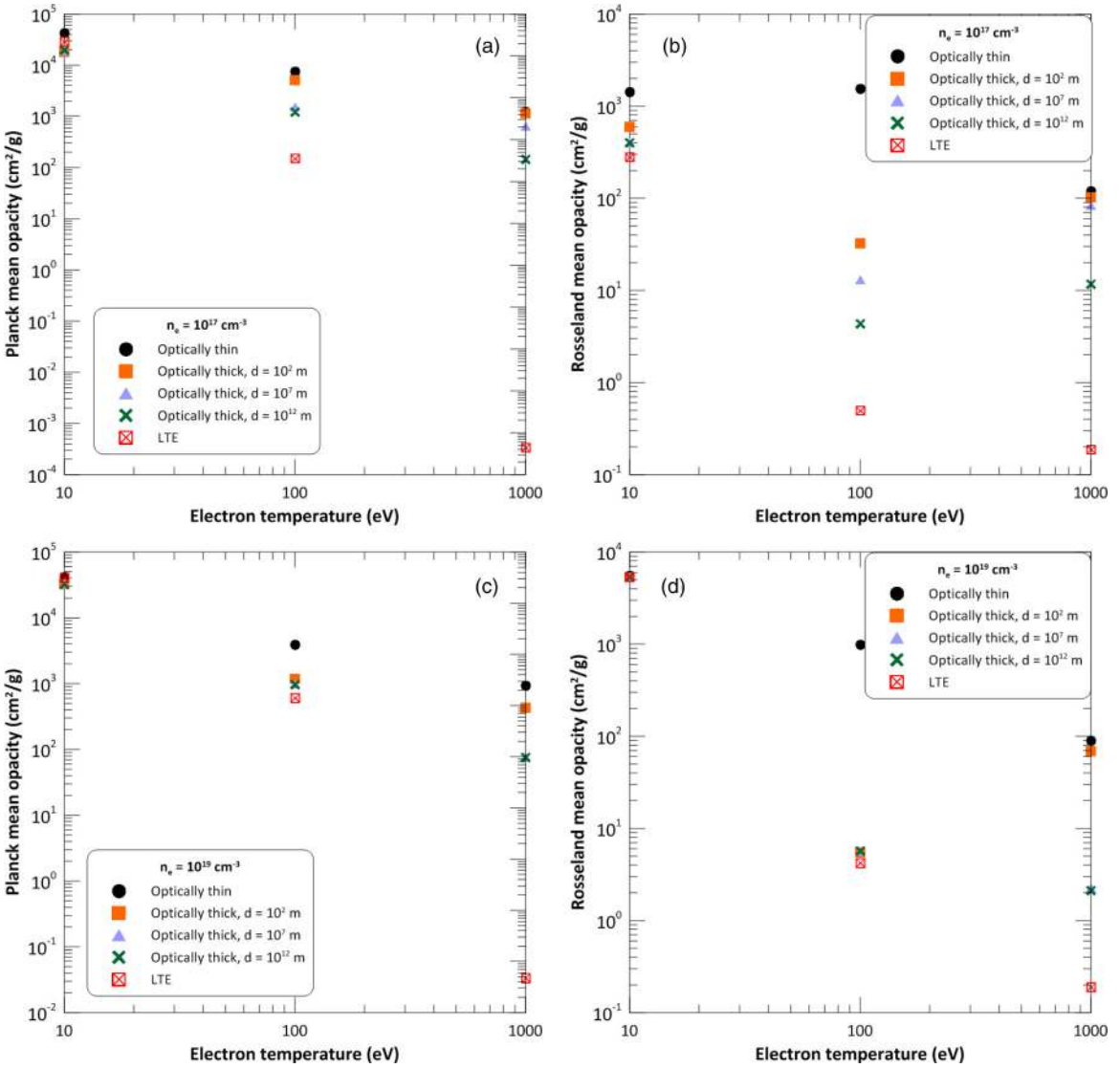

FIG. 12. Comparison of Planck and Rosseland mean opacities of iron plasmas obtained from LTE and NLTE optically thin and thick models at three temperatures and for three plasma lengths.

plasma conditions those differences can reach three or four orders of magnitude.

We have also performed a brief analysis of the influence of plasma self-absorption in the calculation of the radiative properties when the plasma width is considered, assuming planar geometry. Oxygen and iron cases were studied at three electron densities and temperatures and for three plasma slab widths. As expected, we obtained that, at low temperatures, the optically thick results are quite close to those obtained in LTE, especially when the density increases. This is relevant for oxygen since its contribution to the plasma mixture is relevant in that range of electron temperatures. As the temperature increases the agreement between optically thick and LTE results worsens, and at 1000 eV the differences are noticeable. This result is important for iron simulations, since its contribution to the radiative properties of the mixture is more significant for temperatures higher than 100 eV.

ACKNOWLEDGMENTS

This work was supported by the Spanish Government through Project No. FIS2016-81019-P and by the EUROfusion Consortium Task Agreement WPENR: Enabling Research IFE, Project No. AWP15-ENR-01/CEA-02.

[1] K. Schure, D. Kosenko, J. Kaastra, R. Keppens, and J. Vink, Astron. Astrophys. **508**, 751 (2009).
[2] S. Bradshaw and P. Cargill, Astron. Astrophys. **437**, 311 (2005).
[3] F. Reale, Living Rev. Solar Phys. **11**, 4 (2014).
[4] A. Dalgarno and R. McCray, Annu. Rev. Astron. Astrophys. **10**, 375 (1972).

[5] H. Summers and R. McWhirter, J. Phys. B **12**, 2387 (1979).
[6] J. MacDonald and M. Bailey, Mon. Not. R. Astron. Soc. **197**, 995 (1981).
[7] R. Sutherland and M. Dopita, Astrophys. J. Sup. Ser. **88**, 253 (1993).
[8] O. Gnat and A. Sternberg, Astrophys. J. Sup. Ser. **168**, 213 (2007).
[9] B. Smith, S. Sigurdsson, and T. Abel, Mon. Not. R. Astron. Soc. **385**, 1443 (2008).
[10] D. E. Post, R. V. Jensen, C. B. Tarter, and W. A. Lokke, At. Data Nucl. Data Tables **20**, 397 (1977).
[11] K. B. Fournier, M. Cohen, M. J. May, and W. H. Goldstein, At. Data Nucl. Data Tables **70**, 231 (1998).
[12] D. Morozov, E. BaronovaI, and Y. Senichenkov, Plasma Phys. Rep. **33**, 906 (2007).
[13] J. Gil, R. Rodriguez, P. Martel, R. Florido, J. Rubiano, M. Mendoza, A. de la Nuez, G. Espinosa, and E. Minguez, J. Quant. Spectrosc. Radiat. Transfer **125**, 123 (2013).
[14] A. Mavrin, Radiat. Eff. Defect. S. **173**, 388 (2018).
[15] D. Salzmann, *Atomic Physics in Hot Plasmas* (Oxford University Press, Oxford, 1997).
[16] M. Seaton, Y. Yan, D. Mihalas, and A. Pradhan, Mon. Not. R. Astron. Soc. **266**, 805 (1994).
[17] M. Seaton and N. Badnell, Mon. Not. R. Astron. Soc. **354**, 457 (2004).
[18] N. Badnell, M. Bautista, and K. Butler, Mon. Not. R. Astron. Soc. **360**, 458 (2005).
[19] F. Rogers and C. Iglesias, Astrophys. J. Sup. Ser. **79**, 507 (1992).
[20] C. Iglesias and F. Rogers, Astrophys. J. **464**, 943 (1996).
[21] N. H. Magee, J. Abdallah, Jr., R. E. H. Clark, J. S. Cohen, L. A. Collins, G. Csanak, C. J. Fontes, A. Gauger, J. J. Keady, D. P. Kilcrease, and A. L. Merts, in Astropysical Applications of Powerful New Databases, edited by S. J Adelman and W. L. Wiese (Astronomical Society of the Pacific, San Francisco, 1995), Vol. 78, p. 51.
[22] C. Blancard, P. Cosse, and G. Faussurier, Astrophys. J. **745**, 10 (2012).
[23] J. Colgan, D. Kilcrease, N. Magee, M. Sherrill, J. J. Abdallah, P. Hakel, and C. Fontes, Astrophys. J. **817**, 116 (2016).
[24] B. Rozsnyai, J. Quant. Spectrosc. Radiat. Transfer **71**, 655 (2001).
[25] J. Eldridge and C. Tout, Mon. Not. R. Astron. Soc. **348**, 201 (2004).
[26] F. Wang, Z. Gang, and J. Yuan, Astrophys. J. **600**, 963 (2004).
[27] G. Cheng and Z. Jiaolong, Phys. Rev. E **78**, 046407 (2008).
[28] F. Jin, J. Zeng, T. Huang, Y. Ding, Z. Zheng, and J. Yuan, Astrophys. J. **693**, 597 (2009).
[29] S. Turck-Chieze, F. Delahaye, D. Gilles, G. Loisel, and L. Piau, High Energy Density Phys. **5**, 132 (2009).
[30] D. Whittaker and G. Tallents, Mon. Not. R. Astron. Soc. **400**, 1808 (2009).
[31] D. Gilles *et al.*, High Energy Density Phys. **7**, 312 (2011).
[32] S. Turck-Chiéze *et al.*, High Energy Density Phys. **9**, 473 (2013).
[33] J. Bailey *et al.*, Nature (London) **517**, 56 (2015).
[34] D. Gilles, M. Busquet, M. Klapisch, F. Gilleron, and J.-C. Pain, High Energy Density Phys. **16**, 1 (2015).
[35] R. D. Bates, A. E. Kingston, and R. P. McWirther, Proc. R. Soc. London Ser. A **267**, 297 (1962).
[36] S. Hansen, C. Fontes, J. Colgan, J. J. Abdallah, H. Chung, H. Scott, V. Novikov, O. Peyrusse, G. Ferland, R. Williams, and Y. Ralchenko, in *Modern Methods in Collisional-Radiative Modeling of Plasmas*, edited by Y. Ralchenko, Springer Series on Atomic, Optical and Plasmas Physics Vol. 90 (Springer, Berlin, 2016).
[37] J. Bauche, C. Bauche-Arnoult, and M. Klapisch, Adv. At. Mol. Phys. **23**, 131 (1987).
[38] A. Bar-Shalom, J. Oreg, W. H. Goldstein, D. Shvarts, and A. Zigler, Phys. Rev. A **40**, 3183 (1989).
[39] S. Mazevet and J. J. Abdallah, J. Phys. B **39**, 3419 (2006).
[40] S. Hansen, J. Bauche, C. Bauche-Arnoult, and M. Gu, High Energy Density Phys. **3**, 109 (2007).
[41] E. Anders and N. Grevesse, Geochim. Cosmochim. Acta **53**, 197 (1989).
[42] M. Asplund, N. Grevesse, A. J. Sauval, and P. Scott, Annu. Rev. Astron. Astrophys. **47**, 481 (2009).
[43] G. Sacco, S. Orlando, C. Argiroffi, A. Maggio, G. Peres, F. Reale, and R. Curran, Astron. Astrophys. **522**, A55 (2010).
[44] W. Lotz, Z. Phys. **216**, 241 (1968).
[45] M. F. Gu, Can. J. Phys. **86**, 675 (2008).
[46] H. Van Regemorter, Astrophys. J. **136**, 906 (1962).
[47] H. A. Kramers, Philos. Mag. **46**, 836 (1923).
[48] H. R. Griem, *Principles of Plasma Spectroscopy* (Cambridge University Press, Cambridge, 1997).
[49] J. C. Stewart and K. D. Pyatt, Astrophys. J. **144**, 1203 (1966).
[50] K. Nishikawa and M. Wakatani, *Plasma Physics* (Springer, Berlin, 1993).
[51] L. Spitzer, *Physics of Fully Ionized Gases* (Interscience, New York, 1962).
[52] J. J. Abdallah, J. Colgan, and N. Rohringer, J. Phys. B **46**, 235004 (2013).
[53] R. C. Mancini, R. F. Joyce, and C. F. Hooper, Jr., J. Phys. B **20**, 2975 (1987).
[54] M. Klapisch and M. Busquet, New J. Phys. **15**, 015012 (2013).
[55] R. Rodríguez, G. Espinosa, J. M. Gil, J. G. Rubiano, M. A. Mendoza, P. Martel, and E. Mínguez, Commun. Comput. Phys. **16**, 612 (2014).
[56] G. Espinosa, R. Rodriguez, J. M. Gil, F. Suzuki-Vidal, S. V Lebedev, A. Ciardi, J. G Rubiano, and P. Martel, Phys. Rev. E **95**, 033201 (2017).
[57] R. Rodríguez, R. Florido, J. M. Gil, J. G. Rubiano, P. Martel, and E. Mínguez, Laser Part. Beams **26**, 433 (2008).
[58] R. Rodríguez, R. Florido, J. M. Gil, J. G. Rubiano, D. Suárez, P. Martel, E. Mínguez, and R. C. Mancini, Commun. Comput. Phys. **8**, 185 (2010).
[59] D. Mihalas, *Stellar Atmospheres* (Freeman, San Francisco, 1970).
[60] M. S. Dimitrijevic and N. Konjevic, Astron. Astrophys. **172**, 345 (1987).
[61] S. J. Rose, J. Phys. B **25**, 1667 (1992).
[62] R. J. Rütten, *Radiative Transfer in Stellar Atmospheres* (Sterrekundig Instituut Utrecht, Utrecht, 1995).
[63] F. Serduke, E. Mínguez, S. Davidson, and C. Iglesias, J. Quant. Spectrosc. Radiat. Transfer **65**, 527 (2000).
[64] J. M. Gil, R. Rodriguez, R. Florido, J. G. Rubiano, P. Martel, and E. Minguez, Laser Part. Beams **26**, 21 (2008).
[65] J. M. Gil, R. Rodriguez, P. Martel, R. Florido, J. G. Rubiano, M. A. Mendoza, and E. Minguez, J. Quant. Spectrosc. Radiat. Transfer **114**, 136 (2013).

[66] R. Rodríguez, R. Florido, J. M. Gil, J. G. Rubiano, P. Martel, M. A. Mendoza, D. Suárez, and E. Mínguez, J. Phys.: Conf. Ser. **112**, 042002 (2008).
[67] C. Fontes, J. J. Abdallah, C. Bowen, R. Lee, and Y. Ralchenko, High Energy Density Phys. **5**, 15 (2009).
[68] H.-K. Chung, C. Bowen, C. Fontes, S. Hansen, and Y. Ralchenko, High Energy Density Phys. **9**, 645 (2017).
[69] R. R.Piron, F. Gilleron, Y. Aglitskiy, H.-K. Chung, C. Fontes, S. Hansen, O. Marchuk, H. Scott, E. Stambulchik, and Y. Ralchenko, High Energy Density Phys. **23**, 38 (2017).
[70] S. Langer, G. Chanmugam, and G. Shaviv, Astrophys. J. **245**, L23 (1981).
[71] R. Chevalier and J. Imamura, Astrophys. J. **261**, 543 (1982).
[72] J. Kaastra, R. Mewe, and H. Nieuwenhuijzen, in Proceedings of the 11th Colloquium on UV and X-Ray Spectroscopy of Astrophysical and Laboratory Plasmas, edited by Y. Yamashita and T. Watanabe (Universal Academy Press, Tokyo, 1996), pp. 411–414.
[73] H. Chung, M. Chen, W. Morgan, Y. Ralchenko, and R. Lee, High Energy Density Phys. **1**, 3 (2005).
[74] M. Asplund, N. Grevesse, and A. Sauval, in *Cosmic Abundances as Records of Stellar Evolution and Nucleosynthesis in Honor of David L. Lambert*, edited by T. G. Barnes III and F. N. Bash, Astronomical Society of the Pacific Conference Series Vol. 336 (Astronomical Society of the Pacific, San Francisco, 2005), pp. 25–38.
[75] R. Drake, *High Energy Density Physics: Fundamentals, Inertial Fusion and Experimental Astrophysics* (Springer, Berlin, 2005).
[76] G. Withbroe, Centre for Astrophysics, Harvard College Observatory, and Smithsonian Astrophysical Observatory Report No. 524, 1978 (unpublished).
[77] J. Colgan, C. Fontes, and J. Abdallah, Jr., High Energy Density Phys. **2**, 90 (2006).
[78] D. Hummer and D. Mihalas, Astrophys. J. **331**, 794 (1988).
[79] S. Ichimaru, Rev. Mod. Phys. **54**, 1017 (1982).
[80] B. Crowley, High Energy Dens. Phys. **13**, 84 (2014).
[81] D. Mihalas and B. Weibel-Mihalas, *Foundations of Radiation Hydrodynamics* (Dover, New York, 1999).